Synchronization and dynamics of the axisymmetrically excited jet in crossflow

Elijah W. Harris ●, Stephen G. Schein ●, David D. W. Ren, and Ann R. Karagozian ●*
Department of Mechanical and Aerospace Engineering,
University of California, Los Angeles, Los Angeles, California 90095, USA

This experimental study explored the effects of various axisymmetric temporal excitation waveforms on gaseous transverse jet synchronization and dynamical characteristics, vorticity evolution, and molecular mixing. The study focused on the naturally absolutely unstable transverse jet, with a jet-to-crossflow momentum flux ratio $J = 6$, employing simultaneous acetone planar laser-induced fluorescence imaging and stereo particle image velocimetry, enabling new perspectives on the nature of jet control and characteristic signatures associated with optimization. Jet excitation with sinusoidal, square-wave, and double-pulse forcing waveforms was examined, the latter two created with differing numbers of underlying Fourier timescales, and the number of Fourier modes was shown to affect the degree of lock-in of the jet's upstream shear layer to the applied excitation, consistent with an analogous Van der Pol oscillator model. Proper orthogonal decomposition (POD) analysis of the jet's evolving velocity field enabled comparisons of the most energetic mode structures for different excitation conditions and, more significantly, comparisons of various phase portraits associated with three-dimensional plots of the three most energetic POD mode coefficients. Phase portraits revealed significantly different topologies for different excitation conditions, ranging from fairly simple periodic (circular) shapes for sinusoidal excitation to more complex single and multiple loop trajectories for double-pulse forcing with varying degrees of temporal spacing between slow and fast pulses. Subsequent quantification of molecular mixing via acetone PLIF showed that the simpler phase portrait topologies tended to have improved molecular mixing as compared with more complex shapes, but all cases with excitation improved mixing over the unforced transverse jet.

I. INTRODUCTION

The jet in crossflow (JICF) or transverse jet typically consists of a round jet injected perpendicularly into crossflow and can be found in numerous practical engineering systems [1–5]. Even in the case of a single-flush round jet injected into uniform crossflow, the resulting flowfield is inherently complex and dynamically nonlinear, a general representation of which is shown in Fig. 1. Among the dominating JICF flow structures are horseshoe vortices surrounding the jet injection region, upstream shear layer vortices, upright wake vortices, and the counter-rotating vortex pair (CVP) associated with the jet cross-section [6–8]. In this flowfield, a jet with a mean velocity of U_j at the exit plane exhausts into crossflow with a uniform freestream velocity of U_∞. In Fig. 1, the s_c and s curves represent the jet centerline and jet upstream shear layer trajectories, respectively. In characterizing the flowfield, typical nondimensional parameters of interest include the jet-to-crossflow velocity ratio ($R = U_j/U_\infty$), jet-to-crossflow density ratio ($S = \rho_j/\rho_\infty$), jet-to-crossflow momentum flux
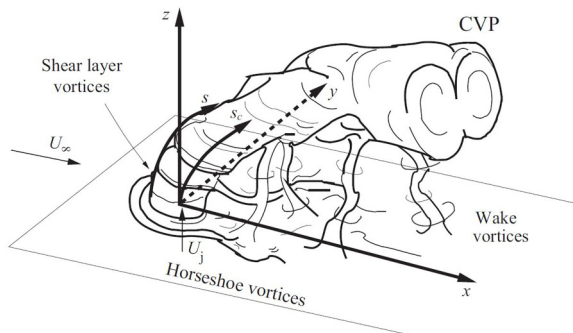
---

*ark@ucla.edu

FIG. 1. Schematic of a flush injected, relative to the injection wall, round jet normal to a transverse flow, with representative depictions of the relevant vortical structures. Appropriate coordinate axes x, y, z, jet shear layer trajectoy s, and jet centerline trajectory s_c are also shown. Adapted from Fric and Roshko [16].

ratio ($J = \rho_j U_j^2 / \rho_\infty U_\infty^2 = SR^2$), and jet Reynolds number ($\mathrm{Re}_j = \rho_j U_j D / \mu_j$), where D is the jet exit diameter and μ_j is the absolute viscosity of the jet. For consideration of the instability characteristics, in particular those along the upstream shear layer (USL) of the jet, the frequency content is nondimensionalized via Strouhal numbers, $\mathrm{St} = fD/U_j$, where the characteristic length scale can also alternatively be defined in terms of the the jet's upstream momentum thickness, θ, rather than the jet's exit diameter. Of the flow structures generated in the JICF, perhaps the most significant are the CVP and the USL vortices, as the latter is associated with the initiation and growth of the former [8–10], and the development, evolution, and eventual breakdown of the CVP has long been understood to be associated with the overall efficacy of mixing between the jet and crossflow [11–13]. The general consensus holds that the CVP originates from a reorientation of azimuthal vorticity in the form of shear layer vortex rings which are folded and tilted by the crossflow as they convect downstream [7,9,14,15].

Based on the dependence of the CVP development on nearfield jet dynamics, numerous studies have focused on the the USL instabilities and associated vorticity close to the transverse jet exit. An important finding documented in extensive experimental studies [17–21] as well as numerical simulations and stability analyses [22–26] is that as the momentum flux ratio J and/or the density ratio S are decreased, there is a critical transition in the jet's USL from being weakly (locally) convectively unstable (CU) to demonstrating strong, pure-tone global instability, with evidence of absolutely unstable (AU) behavior [27]. Recent experimental studies incorporating optical diagnostics [13,20,28] demonstrate that while an AU USL produces a CVP which is typically quite symmetric, when the USL instabilities become weakly convectively unstable, there is a susceptibility for the CVP to develop asymmetrically, with the more symmetric CVP associated with improved molecular mixing of the jet with crossflow. From triglobal stability and adjoint sensitivity analysis of direct numerical simulations (DNS), Regan and Mahesh [29] identify wavemaker regions in which the jet is most susceptible to localized feedback disturbances. For the case of an AU USL, the wavemaker appears to be isolated in the upstream edge of the jet shear layer, while for a CU USL, the wavemaker extends from the upstream edge of the jet azimuthally around the shear layer. These researchers also perform adjoint sensitivity analysis of the flowfield, demonstrating that excitation near the wavemaker regions produces the greatest potential receptivity to actuation. This notion is explored in the passive sense via experiments for the JICF with small fixed tabs placed at various locations within the jet periphery [30], creating such localized disturbances. Experimental findings support the effect of disturbances placed in these different wavemaker regions, which not only affect jet shear layer instabilities, but also CVP structure, dynamics, and mixing characteristics. These studies demonstrate how impactful the upstream and downstream shear layers are to the overall dynamics of the jet, and in addition also highlight the sensitivity of the flowfield to small perturbations of these shear layers, with resulting implications on the overall mixing efficacy.

Numerous studies of the JICF have sought to exploit the sensitivities of the shear layers and subsequent jet evolution through active (temporal) control [17,31–38]. Historically, such control methods have consisted of simple temporal sinusoidal or square-wave axisymmetric excitation, and under specific excitation conditions produce the desired outcome of enhancing jet spread and mixing through promotion of vorticity generation, interaction, and breakdown. Several studies have compared the impact of different forcing waveforms, particularly the effect of sinusoidal versus square-wave excitation in altering jet structure and dynamics [32,36–38]. They note that for an equivalent energy input, e.g., as quantified by the mean-subtracted root mean square (RMS) of the jet velocity excitation, both sinusoidal and square-wave excitation of a CU JICF can be effective in altering the jet structure and improve mixing. Yet when the jet's USL is naturally AU, with strong pure-tone instabilities, sinusoidal excitation is relatively ineffective, while even axisymmetric square-wave forcing at a moderate excitation amplitude can produce distinct alterations to the jet structure, dynamics, and mixing.

More recent experiments by Harris *et al.* [39] examine the effects of controlled vortex generation and, in particular, forced vortex interactions, as created by axisymmetric JICF excitation. The study uses a novel double-pulse forcing waveform applied to the jet established by two distinct temporal square-wave pulses prescribed during a single forcing period, $T = 1/f_f$. The independent control of the distinct pulses allows for altering the strength, celerity, and spacing of the formed vortex rings, selectively controlling the degree of nearfield interaction and breakdown of the vortical structures. Harris *et al.* [39] characterize the type and degree of filling of the vortex rings using the jet's effective nondimensional stroke ratio, L/D, and ring velocity ratio, r_{ring}, for each individual pulse,

$$\frac{L}{D} = \frac{1}{D} \int_0^\tau (u_j) dt, \tag{1}$$

$$r_{ring} = \frac{\Delta U_j}{U_\infty}, \tag{2}$$

where u_j is the mean-subtracted, temporally evolving vertical jet velocity at the exit plane and τ is the temporal pulsewidth of each pulse. For a range of stroke and ring velocity ratios, applied to both naturally CU and AU transverse jets, the study quantifies differences in jet structure and molecular mixing. All forcing conditions are observed to enhance jet spread, penetration, and molecular mixing, though when the jet's upstream shear layer is convectively unstable, conditions promoting vortex collisions provide the greatest enhancement in molecular mixing, whereas in the naturally absolutely unstable JICF, the greatest mixing enhancement occurs when the vortex rings do not interact. While the findings in Harris *et al.* [39] are consistent with the dynamics and mixing of isolated vortex rings in crossflow studied numerically [40], the altered vorticity generation, interplay between vortex interactions/collisions, and the dynamics of the USL and nearfield are not treated in that study.

Other recent studies have explored in detail the dynamical receptivity or lock-in (LI) of the transverse jet to applied forcing, especially for axisymmetric sinusoidal excitation, and such receptivity is relevant to overall jet performance. When attempting to control upstream shear layer vorticity generation via axisymmetric excitation, the jet has to lock-in, or synchronize, to the forcing frequency, f_f, and thereby overcome the frequency of the natural instabilities of the jet, f_o [36,41]. The lock-in phenomenon is known to occur for a range of self-excited, absolutely unstable shear flows, such as low-density free jets [42], and has been demonstrated for the equidensity ($S = 1$) AU transverse jet [36]. But the more recent studies by Shoji *et al.* [41] indicate that the JICF exhibits full lock-in for flow conditions associated with both AU USL behavior (i.e., low J values, $J < 10$) as well as convectively unstable USL behavior (at larger J values). Additional complexities in the shear layer dynamics for a full range of J values are observed. Quasiperiodicity (QP) in the USL response, whereby spectral peaks at frequencies consisting of linear combinations of f_f and f_o, is also observed to take place for excitation conditions outside of lock-in, typically at forcing frequencies frequencies further from f_o and/or very low amplitudes of excitation.

Further experiments using laser diagnostics by Shoji *et al.* [38] demonstrate that sinusoidal excitation has a relatively significant influence on improved mixing for the convectively unstable JICF at larger J values, especially (but not exclusively) when the USL is locked-in to the forcing frequency, but for an absolutely unstable JICF, only clear lock-in conditions enable alterations in the jet structure, with somewhat moderate improvements in molecular mixing. In contrast, square-wave excitation [37] applied at the same overall frequency and amplitude as sinusoidal excitation of the JICF demonstrates a significant influence on the naturally absolutely unstable JICF, where specific stroke ratios within J-dependent ranges can produce deeply penetrating, periodic vortices and/or improved molecular mixing over the unforced jet. This contrasting behavior is not fully understood, though lock-in experiments are not a part of the study by Shoji *et al.* [37], and clearly the temporal pulse width and hence additional time scales in the excitation enable square-wave excitation to have a difference influence.

In light of these earlier findings, the current study sought to provide a deeper examination of the effects of vortex interactions and collisions demonstrated in Harris *et al.* [39] by focusing on nearfield vorticity evolution and the underlying instability coupling dynamics generated by the double-pulse forcing. Both aspects were investigated from the perspective of synchronization analysis, exploring the route to jet USL lock-in for the various excitation waveforms, and evaluating the implications for overarching dynamics, structure, and mixing further downstream. The methodology by which the square-wave-based waveforms were formed, being that of a sum of simple Fourier series contributions, was investigated by systematically attenuating or completely omitting selected Fourier terms. Quantification of jet characteristics was made through nonintrusive laser diagnostics, acetone planar laser-induced fluorescence (PLIF) imaging and simultaneous stereo particle image velocimetry (PIV). Focus here was placed on an equidensity transverse jet with a naturally AU USL at $J = 6$, at a fixed jet Reynolds number of $Re_j = 1800$. This study enabled a systematic exploration of how and why square-wave and double-pulse forcing can be made so effective for jet control as compared with sinusoidal excitation under comparable conditions, and also explored characteristic signatures associated with optimized behavior, refining selection parameters for forcing waveforms which can maximize mixing efficacy.

II. EXPERIMENTAL SETUP AND METHODS

A. Transverse jet tunnel and injector system

This experimental study was conducted in a nonrecirculating low-speed wind tunnel, a schematic of which is given in Fig. 2. To generate the flow through the tunnel, room air was drawn in continuously by a centrifugal blower. The air was then conditioned through a series of screens and honeycomb cells, followed by a 9:1 area contraction leading into the main test chamber. The prescribed flow conditioning was determined to result in turbulence intensity levels of less than 1.5% with a maximum freestream tunnel velocity of $U_\infty = 7.00$ m/s. The main testing chamber consisted of an aluminum 12 cm $\times$ 12 cm $\times$ 82.5 cm rectangular tube, with jet injection through an orifice flush with the bottom wall and cutouts along the side and top walls. Two of the cutouts were fitted with plexiglass panels to allow for optical access into the chamber for imaging of the experiment, while the third cutout in the top of the tube was mounted with a fused silica quartz window to pass the UV and green laser lights into the tunnel. Additionally, when utilizing a hotwire anemometer for characterization of USL spectral content and feed-forward convergence of the acoustic excitation waveforms, a panel with a small cutout was fitted in the side of the tunnel in place of the plexiglass to allow port access to the probe. A combination of black-anodize surface finish along with a matte black heat-resistant coat of paint along the bottom and at other surfaces served to minimize laser light reflections and ablation. Beyond the main test chamber, the tunnel air was passed through an additional wooden diffusing chamber, with dimensions of 30 cm $\times$ 30 cm $\times$ 63 cm, before passing through exhaust ducting into the building exhaust system. The wooden box was fitted with a small window to allow for an end-on camera viewpoint for cross-sectional imaging of the jet flowfield. To
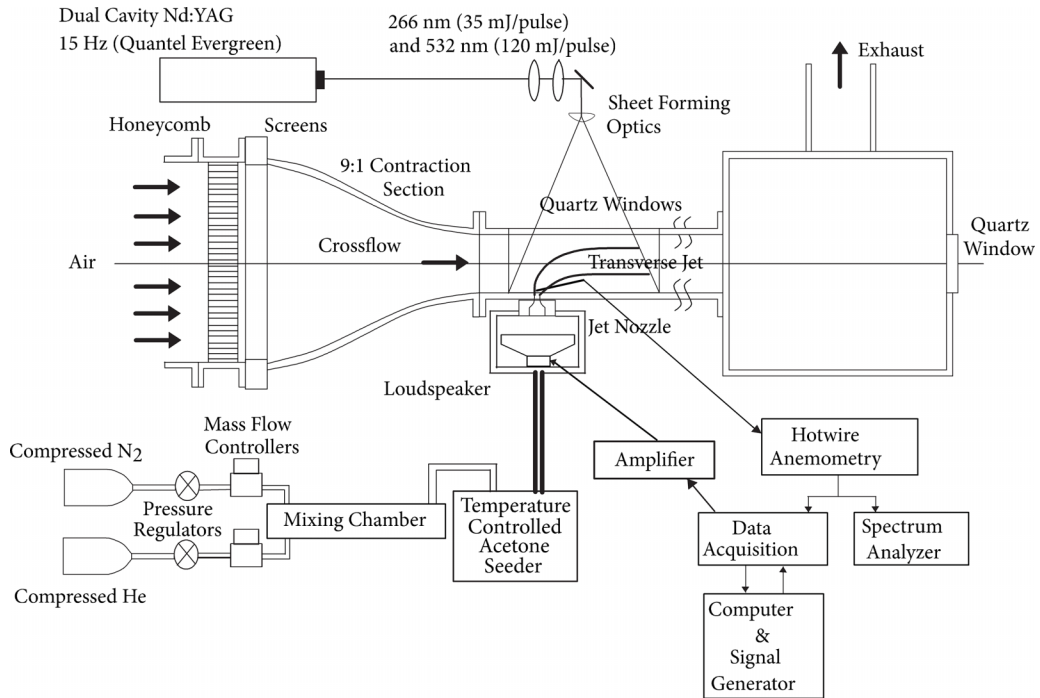
FIG. 2. Low-speed wind tunnel, laser system, hotwire anemometry, and variable-density jet injection comprising the experimental JICF configuration.

accommodate cross-sectional imaging of the jet in crossflow at different downstream locations, the entire experiment and tunnel were affixed to a rail system with stepper motors to enable translation of the experiment relative to the laser sheet, per the discussion below.

Constituent species for the jet fluid were nitrogen, helium, acetone vapor, and di-ethyl-hexyl-sebacat (DEHS) oil ($C_{26}H_{50}O_4$, LaVision 1108951), the latter two of which served as the tracer particles for the PLIF and PIV diagnostics, respectively. The mole fractions of each of the constituent species were utilized along with the room temperature and pressure to establish the bulk fluid properties, the exact determination of which is detailed in Gevorkyan [43]. The He and N_2 flow rates were independently established by two mass flow controllers (Tylan Model FC-260), and when performing simultaneous PLIF and PIV measurements an additional controller (MKS GM50A) was utilized for a secondary supply of N_2 to allow for independent seeding of both tracer particles. For such simultaneous experiments, the He and N_2 flows from the Tylan mass flow controllers were combined in a packed bed mixing chamber and then directed to a temperature-controlled acetone seeding chamber, which was maintained in the vapor phase. The N_2 flow from the MKS flow controller was separately directed to a DEHS atomizing chamber (TSI Model 3076 Constant Output Atomizer) whereby the seeding of the DEHS oil was controlled such that it was sufficiently low to be considered a neutral participant in the overall flow properties of the jet. Adjusting the mole fractions of the other constituent species allowed for careful tuning of the jet Reynolds number, jet density ratio, and jet kinematic viscosity [13,28]. The mole fraction of acetone, ψ, was maintained to lie below the critical saturated vapor concentration to prevent condensation of acetone. For the present experiments, the mole fractions of acetone, He, and N_2 were fixed at 0.112, 0.100, and 0.788, respectively. Flow from the separate seeding chambers was combined and passed to a small plenum upstream of the injection plane, in which a 10.16 cm (4-inch) loudspeaker (RadioShack 40-1022B woofer) was housed; the speaker provided the temporal acoustic excitation of the jet flow. Downstream of the plenum, the jet was injected to the main test chamber through a 16:1 area

contracting nozzle with a fifth-order polynomial surface profile and an exit diameter of 7.59 mm. The nozzle exit plane was mounted flush with the tunnel floor, and produced a near-top-hat velocity profile in the absence of a crossflow. The present experiments had a fixed jet Reynolds number of $Re_j = 1800$, and density ratio of $S = 1.00$, with a bulk jet velocity of $U_j = 3.42$ m/s. In contrast to prior studies examining a range of momentum flux ratios [39], here J was fixed at a value of 6, where the crossflow velocity was fixed at a freestream value in the tunnel of $U_\infty = 1.40$ m/s.

B. Hotwire-based flow characterization and waveform generation

The spectral characteristics at various locations along the USL of the jet (s/D) were measured utilizing a single-component boundary-layer-type hotwire anemometry probe (Dantec 55P15), connected to a 90C10 constant temperature anemometry (CTA) module in a Dantec StreamLine 90N10 frame. Probe access to the flowfield was made via a small port in the side wall of the main test chamber. Traversal of the probe in the x, y, and z directions, with an accuracy of 1 μm (1.32×10^{-4} jet diameters), was possible via Newport high-performance low-profile ball-bearing linear stages constructed in a triple axis traversing platform system. Details regarding the determination of the shear layer trajectory, calibration of the hotwire probe, and other aspects of hotwire utilization may be found in Shoji [44]. Spectral characteristics in the shear layer enabled determination of the state of the USL, i.e., with strong pure-tone instabilities and higher harmonics characteristic of absolute/global instability, or with relatively weakly evolving instabilities and formation of subharmonics and hotwire-based frequency-shifting associated with convective instability in the transverse jet [17–19,21].

Hotwire data were also utilized in nonlinear time-series analysis (NTA) to explore synchronization or lock-in characteristics of the flow in response to the applied forcing. NTA is useful in studying the dynamics of inherently nonlinear physical processes [45]. Though detailed dynamics of the entire JICF were not directly quantified, as it is inherently difficult to measure all relevant state variables to recreate the phase space, an interpretation of the variables' behavior could be made by investigating topological features of phase space reconstructions from time delay embedding of a single variable [46]. This approach was justified since most state variables for a jet are intrinsically coupled to one another [42], and are generally preserving of the original dynamical properties [45]. Here the state variable of interest was the USL vertical velocity as recorded by the hotwire anemometry system. The process for recreating the shear layer dynamics in the phase space followed after the methodologies in Shoji *et al.* [41] for the JICF, Li and Juniper [42] for a hydrodynamically self-excited low-density free jet, and Guan *et al.* [47] for an externally forced self-excited thermoacoustic oscillator. The hotwire-based velocity readings were cast into a d-dimensional Euclidean vector of time delayed elements, where for visual representation of the phase space reconstruction, the first three dimension vectors were plotted against one another. For proper reconstruction and one-to-one projection of the original attractor in the phase space, the embedding dimension was set to be larger than a minimum value, which was determined using Cao's method [48], and the time delay was carefully selected as the first local minimum of the average mutual information function [49].

To explore various temporal waveforms in the jet velocity at the nozzle exit, desired excitation waveforms (sinusoidal, square-wave, and double-pulse square wave) were input to the actuation system. The inputs were produced with a data acquisition (DAQ) board (dSPACE 1104), utilizing ControlDesk software within Matlab's Simulink. The signal was passed to the loudspeaker housed in the plenum upstream of the jet nozzle, and was driven by an amplifier (Adcom GFA-7300) with a constant signal gain of 30. To more precisely form square temporal waveforms at the jet exit, with sharp upsweeps and downsweeps, at a prescribed frequency f_f and duty cycle α, an adaptive feedforward controller described in prior studies was employed [37,39,50]. For double-pulse forcing, the waveform consisted of two independently controllable square-wave pulses which were generated during a single forcing period $T = 1/f_f$. For consistency with earlier double pulse forcing studies [39], a base forcing frequency of $f_f = 55$ Hz was selected here. When performing
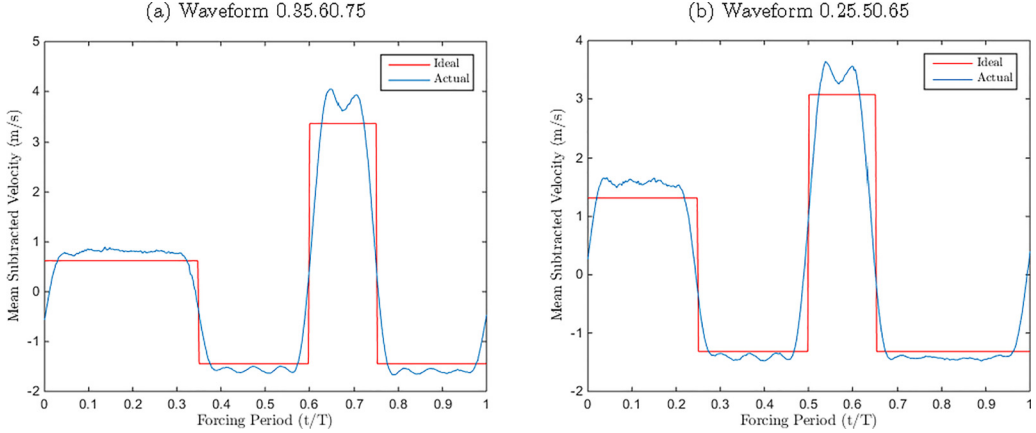
FIG. 3. Representative depictions of actual double-pulse forcing waveforms as compared with their ideal waveforms from the experiments in Harris *et al.* [39].

square-wave and sinusoidal excitation of the jet, forcing frequencies of both $f_f = 55\,\text{Hz}$ and $f_f = 110\,\text{Hz}$ were applied, in that when the double-pulse waveform consisted of two matched and evenly spaced pulses, this was equivalent to simple square-wave forcing at $f_f = 110\,\text{Hz}$. For all forcing cases explored here, the RMS of the velocity perturbation at the jet exit, defined in Eq. (3), was matched so that the effective level of forcing was the same for all cases:

$$u'_{j,\text{rms}} = \sqrt{\frac{1}{T} \int_{t_1}^{t_1+T} (u_j - U_j)^2 dt}. \tag{3}$$

Due to the complex nature of the square-wave and double-pulse forcing waveforms and loudspeaker limitations, the signal for these waveforms was composed of a Fourier series of sinusoids at the fundamental forcing frequency in addition to 14 higher harmonics. Each of the individual Fourier sinusoidal inputs were decomposed into $\sin(k f_f t)$ and $\cos(k f_f t)$ functions, with $f_f = 55\,\text{Hz}$ and $k = 1, 2,..., 15$, so that adjustments in the amplitudes of these functions translated to alterations in the amplitude and phase of the original signal components. Complicating the waveform formation were the inherent nonlinearities of the experimental setup, the imperfect nonflat frequency response of the actuation system, and the nonlinear behavior of the JICF itself [32,33,36,37]. As such, measurements of the resulting excitation waveform were made via hotwire anemometry, with the probe centered over the jet exit at 0.1 diameters above the exit plane, while digital sampling of the analog signal was made at 20 kHz. The largest uncertainties in the velocity fluctuations were on the order of 1% for a velocity of 1 m/s, as documented in prior studies [20]. The recorded waveforms were used in an adaptive feedforward approach to converge to well refined waveforms at the exit plane. Details regarding the waveform formation, the adaptive feedforward method, and the convergence are given in Shoji *et al.* [37] and Harris *et al.* [39].

Figure 3 represents sample double-pulse forcing waveforms, including ideal as well as their final converged waveforms, the latter as measured by the hotwire anemometer just above the jet exit. These cases both have a mean subtracted perturbation amplitude of $u'_{j,\text{rms}} = 2.00$ m/s. The naming convention for the double-pulse forcing is described in detail in Harris *et al.* [39], deriving from the initiation and termination of the two square-wave pulses during a single forcing period. For Fig. 3(a), for example, the waveform was designated as 0.35.60.75, indicating that the first pulse initiated at $t/T = 0.0$ and terminated at $t/T = 0.35$, with a duration of $\tau_{\text{input},1}/T = 0.35$, while the second pulse initiated and terminated at $t/T = 0.60$ and $t/T = 0.75$, respectively, creating a pulse duration of $\tau_{\text{input},2}/T = 0.15$ and a temporal delay after the first pulse of $\Delta\tau_{1\to2}/T = 0.25$. While the converged waveforms had some slight ringing at the peaks, overall each of the pulses

had relatively clean and sharp upsweeps and downsweeps, as the essential features for squarelike excitation for the JICF [35,37]. Such waveforms are shown to create appropriate flow structures at the jet exit, enabling controlled vortex collisions, grazing, or completely independent formation and evolution [39]. While the present study explored various double-pulse square waveforms with all 14 higher harmonics, in other cases the number of Fourier terms was varied, with different cases limiting the total to include only 2, 5, or 10 terms, and in some cases not always sequential terms, as will be discussed below. These truncated series were studied to examine the influence of the number of harmonics on the dynamical character of the forced transverse jet in addition to its influence on the nature of synchronization. We note that fewer terms in the Fourier series resulted in many cases in more pronounced ringing in the waveforms.

C. Optical diagnostics and metrics

In addition to hotwire anemometry, nonintrusive acetone planar laser-induced fluorescence (PLIF) imaging and stereo particle image velocimetry (PIV) served as the main tools for investigating JICF characteristics. Figure 2 includes the general optical configuration when simultaneous PLIF and PIV imaging was performed along the jet centerplane. The light source for both diagnostics was a dual-cavity Q-switched Nd:YAG laser (Quantel Evergreen 30266) operating at wavelengths of 532 nm (visible green) and 266 nm (UV), utilized for the PIV and PLIF imaging, respectively. The resulting collimated green and UV laser beam was first passed through a focusing optic, followed by a turning mirror to redirect it toward the test-section, and ultimately passed through a UV optimized cylindrical lens with $f = -10$ mm to spread the laser into a thin laser sheet just prior to entering into the tunnel. The cylindrical lens could be rotated so that the sheet was aligned along either the jet centerplane or cross-section, while the focusing optic was configured so that the focal point of the laser was maintained just above the tunnel floor. This focal point location was found to produce a sufficiently thin laser sheet of $\approx$1.2–1.4 mm throughout the entire field of view (FOV), as measured by the knife edge technique. This sheet thickness was sufficiently thick to capture out of plane particle movements in the PIV imaging, allowing for resolved three-component velocity vectors, yet thin enough to evaluate the flowfield assuming a planar measurement. In a few cases, high resolution PLIF imaging was performed without simultaneous PIV, where the collimated laser beam was passed through two dichroic mirrors, to split the UV component from the green and improve the overall UV to green signal-to-noise ratio (SNR), before passing through the focusing optic. Additionally, the UV light was passed through a UV-grade fused silica window which reflected a portion of the laser ($\approx$7 %) to a pyroelectric joulmeter (Newport 818E-10-50-S) for shot-to-shot energy measurements, utilized later in PLIF imaging post-processing.

While the laser system was capable of operating at a maximum repetition rate of 15 Hz, the experiments were conducted at approximately 5 Hz to prevent excessive ablation and reflections at the laser floor from the higher energy green light, and to maximize the SNR of the UV to green light. The exact operating frequency was established at 5.01 Hz such that when the JICF was synchronized to the excitation waveforms, at base forcing frequencies of $f_f = 55$ Hz or $f_f = 110$ Hz, the resulting image snapshots were pseudo phase advancing due to the stroboscopic effect. In the case of synchronized forcing at a frequency of $f_f = 55$ Hz, the laser repetition rate resulted in successively recorded images which were separated by a phase difference of $\approx$2.5°, resulting in approximately 144 images recorded over one temporal period. While each laser cavity was able to produce laser pulses at 8 ns full width at half maximum with UV and green energy levels of approximately 30 and 200 mJ, respectively, the system was generally operated at off-maximum conditions to further mitigate ablation and reflections at the laser floor, and to allow for individual tuning of the cavities to precisely match the intensity of illumination within the optical FOV. This latter aspect was important in post-processing of the PIV snapshots to yield accurate extraction of velocity vectors, especially with respect to the out of plane velocity when resolving all 3 velocity components in stereo PIV. The repetition rate, time increment between the cavities, and timing of the laser relative to the cameras were all controlled by a programmable external timing unit and LaVision's DaVis 8.2 software.

For these optical diagnostics, acetone vapor served as the tracer for the PLIF imaging, and DEHS oil ($C_{26}H_{50}O_4$, LaVision 1108951) was used as the tracer for PIV measurements. Additionally, when conducting PIV experiments, glycol-based smoke particles (0.2 μm mass-median diameter) were added to the crossflow by a commercial grade fog machine (Pea Soup Rocket) just outside of the centrifugal blower to visualize and quantify the crossflow velocity field. The acetone mole fraction in the jet was fixed in these experiments at $\psi = 0.112$, maximized within plumbing/flow constraints to improve the contrast between the seeded jet and nonseeded crossflow. The PIV tracers were seeded in such nominal amounts that they were assumed to be neutral, massless participants in the flowfield. Simultaneous PLIF/PIV imaging was performed in the jet centerplane (x-z plane) and at cross-sectional locations in y-z planes near the jet exit, at downstream locations $x/D = 0.0$ and $x/D = 1.0$; additional locations are documented in Ref. [51]. In contrast, the high resolution PLIF imaging was performed at jet cross-sectional locations further downstream, at $x/D = 1.5$, $x/D = 2.5$, and $x/D = 5.5$. At these locations, the dominant velocity component was out of plane, rendering PIV ineffective and thus freeing the PIV cameras (LaVision Imager ProX) to be repurposed for the PLIF imaging, also performed with a jet acetone mole fraction of 0.112. Improved camera resolution and intensifier performance, in addition to the aforementioned improvement in the SNR for UV to green SNR, enabled improved overall resolution.

In all of the imaging data sets, 600 instantaneous snapshots were acquired, well above that necessary to provide statistical convergence [44]. For the simultaneous imaging, a 12-bit internally intensified CCD camera (LaVision NanoStar) with image resolution of 1280×1040 pixels was utilized for the PLIF images and two 14-bit cross-correlated CCD cameras (LaVision Imager ProX) were utilized for the stereoscopic PIV images. When imaging along the centerplane of the jet, all of the cameras were oriented along the side optical window of the tunnel, where the PLIF camera was positioned perpendicular to the x-z plane, and the PIV cameras, positioned on either side of the PLIF camera, were at angles displaced from perpendicular to the x-z plane of approximately 22.5°, with the resulting offset yielding a 45° separation between the two cameras. The PLIF camera was affixed with a Sigma 90 mm AF lens at $f/2.8$, with an accompanying Vivitar $+2$ dioptre close-up lens, and a bandpass filter to isolate light in the acetone fluorescence spectrum from that of other irradiated background light. The internal intensifier on the NanoStar camera was operated at a gate time of 200 ns, corresponding to an exposure time that was 1% of the lifetime for phosphorescence of acetone molecules. Separately, the PIV cameras were each mounted with a Nikon 60 mm lens at $f/11.0$, coupled with a 532.5 nm narrowband filter. To assist in the fine tuning of the PIV imaging, a Scheimpflug lens mount (LaVision 1108196 version 1) was integrated with the lenses, allowing for tilting of the lens plane relative to the CCD array to maintain focus over the entire domain. Post-processing of the PLIF images included 2×2 binning, noise bias correction, flat-field correction, background subtraction, laser energy absorption correction, and a dual-pass filtering. Details regarding these processes, and representative effects on the images, are documented in Shoji [44]. For the simultaneous imaging, shot-to-shot energy corrections could not be implemented due to the presence of the green light, which saturated the energy meter. Post-processing of the PIV images was self-contained within LaVision's DaVis 8.2 software, where user defined parameters afforded the selection of vector calculations via a multipass stereo cross-correlation with a decreasing window sizing of interrogation for improved accuracy (two passes at 32×32 pixel interrogation area at a 50% overlap, and four passes at 24×24 pixel area at a 75% overlap).

In performing cross-sectional simultaneous imaging, the cameras were instead aligned with the PLIF camera at the end of the test section oriented through an optical port in the settling chamber of the tunnel, and the PIV cameras were aligned on either side of the tunnel with the same offset angles of approximately 22.5° from perpendicular to the yz plane. While the PIV camera lens and filter mounts were exactly the same as detailed for the centerplane imaging, due to the longer focal point necessitated for the PLIF camera, the Sigma 90 mm AF lens at $f/2.8$ was swapped out for a Nikon 200 mm lens at $f/4.0$. Post-processing of both PLIF and PIV images remained consistent with procedures already detailed.

High-resolution PLIF images were recorded with a 14-bit charge coupled device (CCD) camera (LaVision Imager proX) with image resolution of 1600×1200 pixels, with an extermal image intensifier (LaVision IRO) to improve SNR. In the present study, only cross-sectional high-resolution PLIF images at $x/D = 5.5$ are shown, principally to enable structural comparisions to nearfield PIV-based cross-sectional vorticity in the jet. Separate studies [39,51] contain extensive datasets for high-resolution PLIF for the present excitation cases, including molecular mixing quantification in the centerplane and cross-sectional planes.

In the present studies, as in other recent transverse jet experiments [13,30,37–39,52], the unmixedness parameter was used in quantifying the molecular mixing of the jet and crossflow fluid [53]. The unmixedness quantifies molecular mixing via statistics associated with the second moment or variance of the scalar field, and can be represented by Eq. (4), for example, when evaluated at a downstream location x, extracted from a thin slice of a PLIF image in the x-z plane (centerplane):

$$U_{xz} = \frac{1}{L_x L_z} \int \int \frac{\left(\frac{C}{C_o} - \frac{\overline{C}}{C_o}\right)^2}{\frac{\overline{C}}{C_o}\left(1 - \frac{\overline{C}}{C_o}\right)} dx dz. \tag{4}$$

Here C represents a local pixel element concentration associated with acetone fluorescence within an instantaneous jet image, $\overline{C}$ represents the spatially averaged concentration over the entire interrogation area, and C_o is the concentration value at the jet exit, in the potential core region, which is applied as a scaling factor. The unmixedness is essentially a spatial variance measurement, normalized by the variance obtained when the flow field is stirring but not mixing or diffusing [54]. $L_x L_z$ represents the physical size of the interrogation area where the analysis is being performed, in this case, a thin (7 pixel-wide) slice of the jet in its centerplane. To accomplish direct comparisons of molecular mixing metrics in the present experiments among different excitation cases and flow conditions, the size of the overall interrogation area was varied such that the mean value of the scalar over this area, $\bar{C}$, was matched among different cases and at different instants of time [13]. With this mixing metric, lower unmixedness values correspond to improved relative molecular mixing.

III. RESULTS

As noted above, the present study expanded on the high resolution acetone PLIF imaging in Harris *et al.* [39], focusing on the nature of the excitation waveforms and the influence of alternative numbers of Fourier modes on jet dynamical features. As such, the simultaneous PLIF/PIV diagnostics required slight alterations in the proportions of jet constituent species to optimally achieve simultaneous imaging. While the primary flow conditions in Harris *et al.* [39] involve a naturally absolutely unstable USL with $J = 7$ and acetone mole fraction $\psi = 0.218$ (with the same large nozzle), the present studies focused on $J = 6$ and $\psi = 0.112$. From the detailed explorations in Shoji *et al.* [21], it is known that these subtle changes in the jet constituent species concentrations and flow properties can produce alterations in the transverse jet's USL instability characteristics. Figure 4 depicts the spectral characteristics associated with the USL for the present studies, represented by a contour plot of the hotwire-detected magnitude and frequency of the USL instabilities for the unforced jet as a function of the distance s/D. While the spectral character here indicated a broader peak than is typical for AU behavior, with somewhat weaker side lobes, the relatively strong pure-tone instability, initiating at around $s/D = 0.5$, and the absence of subharmonics and presence of higher harmonics, nevertheless suggested an AU USL for this case. Interestingly, while the present flow conditions produced a dominant frequency of $f_0 = 375$ Hz for $J = 6$ and $\psi = 0.112$, for the AU case in Harris *et al.* [39], $f_0 = 540$ Hz with $J = 7$ and $\psi = 0.218$. The decrease in the dominant fundamental frequency was consistent with trends for a smaller flush nozzle described in Shoji *et al.* [21], resulting from a lowered momentum flux ratio (just below the transition from CU to AU) and the decrease in acetone mole fraction while maintaining all other flow conditions as fixed.
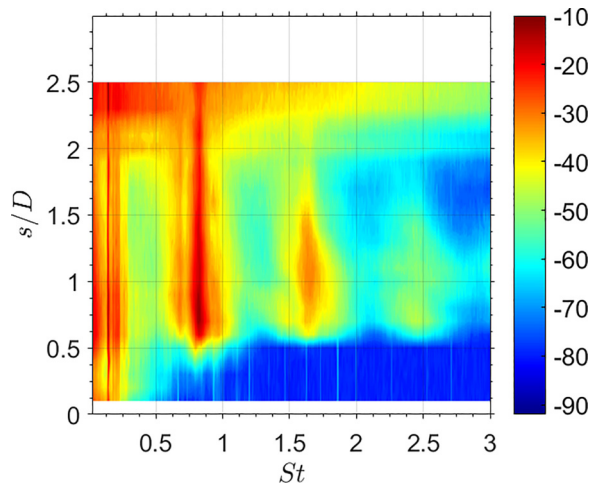
FIG. 4. Power spectral contour plot of the upstream shear layer instabilities for the present flush nozzle-injected JICF with acetone mole fraction of $\psi = 0.112$, $\mathrm{Re}_j = 1800$, and jet velocity of $U_j = 3.42$ m/s at a momentum flux ratio of $J = 6$.

A. Waveform generation and synchronization

1. Experimental lock-in

The lock-in characteristics of the AU JICF were explored for a range of excitation amplitudes and for alternative waveforms including simple sinusoidal and square waves, in addition to double-pulse square waves with differing numbers of harmonic terms in the Fourier series used to create the waveform (see Sec. II B). In these studies, to investigate the effect of the number of harmonic terms, the original 15-term waveform along with truncated 2-, 5-, and 10-term waveforms were generated and compared against simple sinusoidal excitation at $f_f = 55$ Hz and $f_f = 110$ Hz. To determine whether the USL was locked-in (LI), quasiperiodic (QP), or possibly having no significant response (NSR) to the applied forcing, hotwire-based power spectral density (PSD) plots and phase portraits were obtained from time-series vertical velocity data acquired at a given location, $s/D = 1.5$. Velocity measurements at 3 sequential instants of time were used to produce a 3D plot in which multiple physical states were recast into a trajectory representing the time evolution of the state of the flow. The resulting topology of the phase portraits thus represented the type of attactor associated with shear layer dynamics [41,42]. The lowest applied excitation amplitude in the present experiments involved a normalized perturbation magnitude of $u'_{j,\mathrm{rms}}/U_j = 2\%$. The excitation amplitude was systematically increased at increments of $\Delta u'_{j,\mathrm{rms}}/U_j = 5\%$, to a maximum input of $u'_{j,\mathrm{rms}}/U_j = 16\%$, beyond which the jet was able to lock-in to nearly all waveforms considered, including sinusoidal excitation.

Figure 5 depicts sample PSD plots and phase portraits for representative cases of NSR, QP, and transitional QP/LI behavior for sinusoidal forcing of the jet at 55 Hz, and LI behavior of the jet for sinusoidal forcing at 110 Hz. In the absence of any forcing, the spectral characteristics were those shown in the contour plot (Fig. 4) corresponding to the location $s/D = 1.5$. For sine wave forcing at 55 Hz, an excitation amplitude of $u'_{j,\mathrm{rms}}/U_j = 2\%$ produced NSR [Fig. 5(a)], with spectral characteristics essentially identical to USL spectra without any excitation, with the exception of a single isolated spectral peak at the forcing frequency 55 Hz. The corresponding phase portrait [Fig. 5(b)] depicted a typical closed loop trajectory indicative of a simple limit cycle attractor, as expected for a naturally AU flow with a strong pure-tone instability frequency along the USL. As the forcing was increased slightly, to 10%, cases of QP behavior arose, which in the PSD [Fig. 5(c)] showed spectral peaks of competing strengths at linear combinations of the fundamental
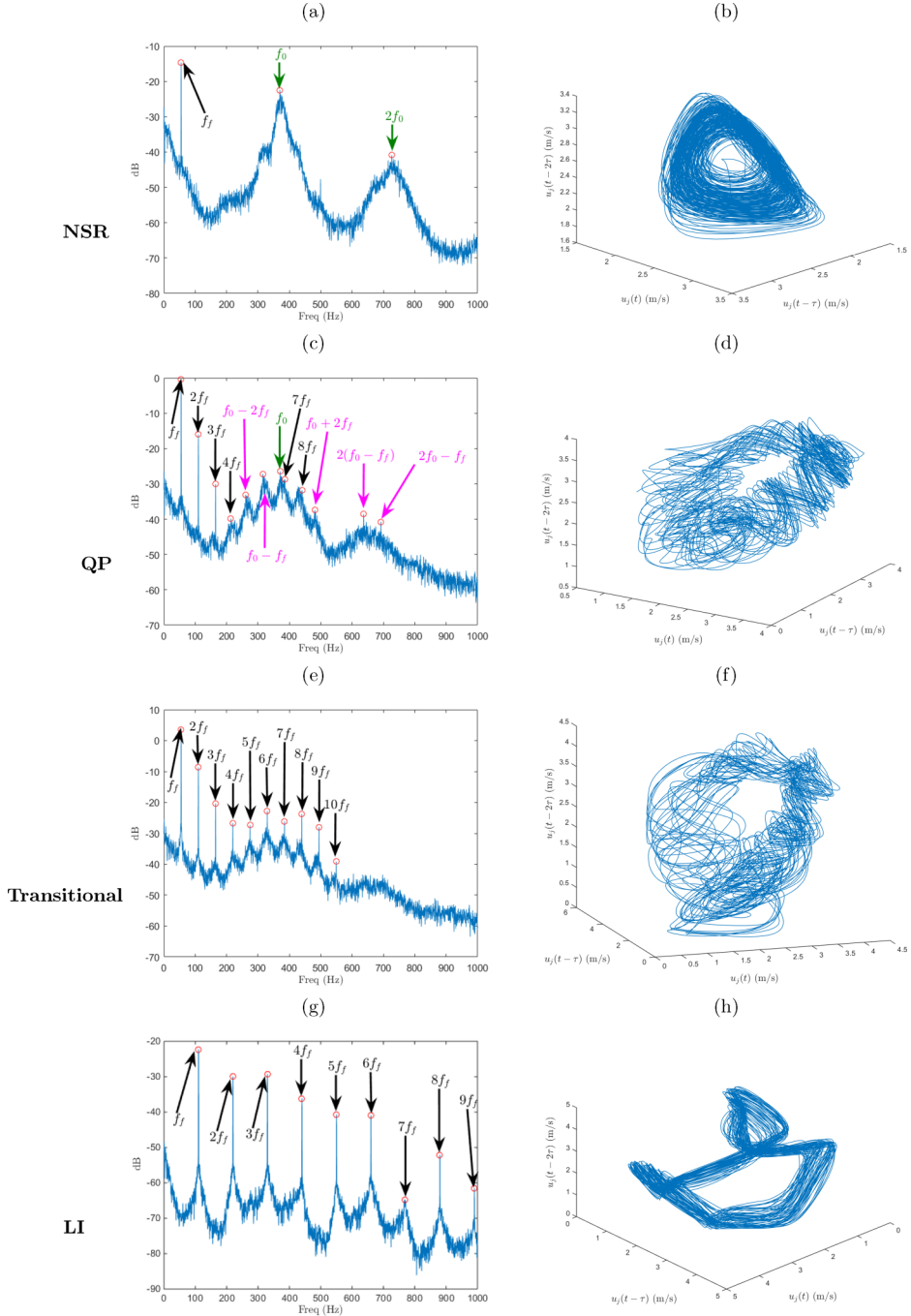
FIG. 5. Examples of spectral characteristics and phase portraits extracted from hotwire-based vertical velocity measurements at $s/D = 1.5$ in response to sinusoidal excitation at 55 Hz (a–f) and 110 Hz (g, h). Amplitudes and responses correspond to $u'_{j,\mathrm{rms}}/U_j = 2\%$, with NSR (a, b); $u'_{j,\mathrm{rms}}/U_j = 10\%$, with QP (c, d); $u'_{j,\mathrm{rms}}/U_j = 16\%$, with transitional response (e, f), and $u'_{j,\mathrm{rms}}/U_j = 16\%$, with LI at $f_f = 110$ Hz (g, h). PSD spectral peaks in black correspond to f_f and higher harmonics, green to f_o and higher harmonics, and pink for linear combinations of the two frequencies.

TABLE I. Experimentally derived synchronization characteristics for the JICF with different forcing waveforms for increasing amplitudes of excitation ($u'_{j,\mathrm{rms}}/U_j$). Shown is the state of the upstream shear layer, designated as having no significant response (NSR), quasiperiodicity (QP), or lock-in (LI). Square waveforms were created from the function generator and feedforward controller, with a base frequency of $f_f = 110$ Hz and differing numbers of Fourier terms. The double pulse square waveform was created with a base frequency of $f_f = 110$ Hz and a 15-term Fourier series.

Amplitude ($u'_{j,\mathrm{rms}}/U_j$)	0.02	0.029	0.044	0.058	0.073	0.088	0.102	0.117	0.132	0.146	0.161
Sinusoidal											
55 Hz	NSR	NSR	QP	QP	QP	QP	QP	QP	QP	QP	QP
110 Hz	QP	QP	QP	QP	QP	QP	LI	LI	LI	LI	LI
Square-wave Fourier modes											
$\alpha = 30\%$, 2 terms	NSR	NSR	QP	QP	QP	QP	QP	QP	QP	LI	LI
$\alpha = 30\%$, 5 terms	QP	QP	QP	QP	QP	LI	LI	LI	LI	LI	LI
$\alpha = 30\%$, 10 terms	QP	QP	LI	LI	LI	LI	LI	LI	LI	LI	LI
$\alpha = 30\%$, 15 terms	QP	QP	LI	LI	LI	LI	LI	LI	LI	LI	LI
$\alpha = 50\%$, 15 terms	LI	LI	LI	LI	LI	LI	LI	LI	LI	LI	LI
Double-pulse											
0.35.65.80, 15 terms	LI	LI	LI	LI	LI	LI	LI	LI	LI	LI	LI

instability frequency f_o and the forcing frequency f_f. In the phase portrait [Fig. 5(d)], QP behavior produced the appropriate form of a toruslike loop, where the phase trajectory was a nonrepeating, nonintersecting closed path representative of the coupling between the two dominant frequencies [42]. Interestingly, with a slight increase in the forcing amplitude to $u'_{j,\mathrm{rms}}/U_j = 16\%$, the PSD in Fig. 5(e) suggested clear lock-in to the forcing, since there was no trace of the fundamental f_o in the spectra. Yet the phase portrait [Fig. 5(f)] showed a portion of the trajectory which still depicted toruslike behavior, hence this condition was deemed to be transitional between QP and LI. In contrast, sinusoidal forcing at $f_f = 110$ Hz at the same forcing amplitude of $u'_{j,\mathrm{rms}}/U_j = 16\%$ was found to produce LI characteristics in both spectra [Fig. 5(g)] and phase portraits [Fig. 5(h)]. In the case of the former, the jet shear layer completely forewent the natural instabilities and was solely characterized by the dynamics of the forcing frequency and its higher harmonics. In the phase portrait [Fig. 5(h)], the trajectory had a clear closed loop path, characteristic of a limit cycle attractor, which indicated a singular dominant frequency along the shear layer, but with an unusual small loop in the topology. These general traits were observed in a range of alternative waveforms and excitation conditions. Given the complexity of visually interpreting the phase portraits, and the corresponding possibility of false-positives in PSD plots, both metrics were used in characterizing the synchronization behavior of the jet.

Table I lists the types of waveforms explored in the synchronization dynamics experiments and the state of the USL as determined from PSD plots and phase portraits, described above. Here forcing amplitudes ranged from $u'_{j,\mathrm{rms}}/U_j = 0.02$ to $u'_{j,\mathrm{rms}}/U_j = 0.16$, and response to sinusoidal excitation was compared with square waveforms at duty cycle $\alpha = 30\%$, with different numbers of Fourier terms, and with an additional double-pulse square-wave case. Interestingly, sinusoidal forcing applied at $f_f = 110$ Hz locked-in the jet shear layer much more easily than sinusoidal forcing at the same amplitudes but at frequency $f_f = 55$ Hz, as shown in the example in Fig. 5. This observation was consistent with findings in Ref. [41] for the JICF under different flow conditions, whereby sinusoidal forcing at a frequency closer to the fundamental instability of the jet (here, $f_o = 375$ Hz) required a lower amplitude to produce lock-in than for f_f further away from f_o.

In the case of square-wave excitation, systematically increasing the number of Fourier series harmonic terms in the waveform acted to significantly reduce the forcing amplitude required to achieve lock-in, at least for a duty cycle $\alpha = 30\%$, likely due to the presence of additional forcing components at increasing frequencies closer to the fundamental. This is confirmed in the table, for

example, by comparing the 5-term and 10- or 15-term square-wave responses to forcing. We note that the waveform associated with 5 Fourier modes was composed of harmonics which all lay below the fundamental frequency, f_o, but the square wave with 10 or 15 Fourier terms had components lying both above and below f_o, providing the ability for the higher frequency components to achieve lock-in more easily, resulting in a lower required amplitude. For example, the results in the table indicated that the 10 term square wave only required half of the relative velocity perturbation, $u'_{j,\mathrm{rms}}/U_j = 0.044$, as the 5-term waveform did ($u'_{j,\mathrm{rms}}/U_j = 0.088$) to achieve lock-in of the USL.

Other interesting observations in Table I include a comparison of the two term Fourier composition of the $\alpha = 30\%$ duty cycle square-wave case, composed of two sinusoids at 55 Hz and 110 Hz, with simple sine wave forcing at 55 Hz and 110 Hz. The two-term square waveform required a higher amplitude of forcing to achieve lock-in than the single sine wave forcing at 110 Hz, but required a lower amplitude to achieve LI than for the sine wave at 55 Hz. As with the earlier example, excitation with a greater contribution at a forcing frequency closer to the fundamental can improve lock-in. Lock-in differences among the 15-term Fourier series waveforms in Table I (square waves with duty cycles of 30% and 50%, and a double-pulse square wave at $\alpha = 50\%$ with characteristics denoted by 0.35.65.80) are also of interest. While the latter two waveforms were already locked-in at the lowest possible forcing amplitude, $u'_{j,\mathrm{rms}}/U_j = 0.02$, the square wave at $\alpha = 30\%$ required a larger amplitude for LI, $u'_{j,\mathrm{rms}}/U_j = 0.044$. Hence, while each of these waveforms was composed of the same Fourier terms, their individual component amplitudes and the nonlinear interactions among them clearly played an important role in achieving jet synchronization. These and related observations help in part to explain previously observed responses of the transverse jet to sine wave and square-wave excitation, where at the same amplitude of forcing, the latter can overcome the dynamics of a JICF with a a naturally absolutely unstable USL, enabling significantly altered jet structure, but the former waveform imparts minimal changes to the AU jet [32,36,37]. Distinct vorticity production via the square wave, however, also plays a role in such observations.

2. Van der Pol oscillator model

A simple modeling effort enabled further interpretation of the dependence of USL synchronization dynamics on the nature of the waveform and number of Fourier terms, such as in Table I, in addition to differences between the ideal and actual waveforms produced (e.g., as in Fig. 3). Shoji *et al.* [41] demonstrates that such synchronization for the self-excited absolutely unstable JICF can be represented through a forced Van der Pol (VdP) oscillator model, as also explored by Li and Juniper [42] for low-density and reactive-free jets. The standard forced Van der Pol oscillator with a driving function is one of the simplest models associated with self-excited temporal solutions, and is known to correspond well to dynamics associated with quasiperiodicity and lock-in phenomena. While these earlier investigations only consider a VdP oscillator forced by a sinusoidal waveform, it has been shown that alternative forcing scenarios may be explored, such as square waves or even random excitation, given that the forcing term is nondiscriminatory with respect to the type of input [55,56]. Hence, for the present study, the forced VdP modeling was extended to a JICF under square-wave excitation to help to provide greater clarity in the underlying mechanisms of the above-noted experimental synchronization.

The forced VdP oscillator is given mathematically by Eq. (5), where z is the dynamical variable of interest, ω_0 is the natural frequency of the self-excited system, and ϵ is the feedback parameter, controlling the degree of linear self-excitation and nonlinear self-limitation in the system. The right-hand side of the equation contains an arbitrary forcing function, $f(t)$, which will take the form of a sine wave in addition to Fourier series compositions representing a square wave, similar to the cases explored in the experiments. Here B may be thought of as the relative applied forcing amplitude for excitation of the system; in the absence of external forcing, where $B = 0$, the system modeled by the VdP oscillator contains a weak nonlinearity with a perfectly circular phase trajectory in the phase space for the condition $\epsilon \ll 1$ [41]. For simplicity, in this investigation the ϵ parameter was chosen to be the same value as that extracted from experiments in Shoji *et al.* [41], $\epsilon = 0.41$. The flow

TABLE II. Tabulation of the normalized critical forcing amplitude $B_{cr}/B_{cr,sine}$ for synchronization of the VdP oscillator model to square-wave forcing with the ideal waveform, and approximated waveforms with sequential 5, 10, and 15 Fourier terms. Waveforms were generated at forcing frequencies of 55 Hz and 110 Hz, for duty cycles of 0.1, 0.2, 0.3, 0.4, and 0.5.

$f_f = 55$ Hz	$\alpha = 10\%$	$\alpha = 20\%$	$\alpha = 30\%$	$\alpha = 40\%$	$\alpha = 50\%$
Fourier, 5 terms	0.370	0.496	0.597	0.749	0.739
Fourier, 10 terms	0.336	0.437	0.496	0.613	0.613
Fourier, 15 terms	0.336	0.437	0.504	0.613	0.622
Ideal waveform	0.109	0.193	0.235	0.303	0.319
$f_f = 110$ Hz	$\alpha = 10\%$	$\alpha = 20\%$	$\alpha = 30\%$	$\alpha = 40\%$	$\alpha = 50\%$
Fourier, 5 terms	0.333	0.365	0.542	0.677	0.522
Fourier, 10 terms	0.354	0.385	0.552	0.688	0.563
Fourier, 15 terms	0.354	0.385	0.563	0.698	0.573
Ideal waveform	0.115	0.177	0.250	0.323	0.260

conditions in that study ($J = 7$, $Re_j = 2300$, $D = 4.04$ mm, and $\psi = 0.218$) are slightly different from those treated here, though Shoji *et al.* [21] demonstrates for arange of jet Reynolds numbers and acetone mole fractions that the JICF instability characteristics are quite similar qualitatively, and when nondimensionalized appropriately, quantitatively as well. As such, for qualitative comparisons of the VdP oscillator model with the experimental synchronization characteristics, the feedback parameter ϵ was assumed to be reasonably accurate in depicting the degree of linear and nonlinear behavior in the jet. The second-order ODE in Eq. (5) is solved using a multiple variable-order algorithm following the procedure in Shoji *et al.* [41] and Li and Juniper [42]:

$$\ddot{z} - \epsilon(1 - z^2)\dot{z} + \omega_0^2 z = Bf(t). \tag{5}$$

To compare this analysis with the experimentally derived lock-in characteristics, the VdP oscillator model explored simple square-wave excitation at forcing frequencies of $f_f = 55$ Hz and $f_f = 110$ Hz, comparing an ideal square wave with approximated square waveforms composed of the first 5, 10, and 15 Fourier terms. The VdP oscillator also examined a range of duty cycles ($\alpha = 0.1, 0.2, 0.3, 0.4$, and 0.5), as well as the impact of skipping over select terms in the Fourier series to further examine the significance of the individual terms and their nonlinear interactions for synchronization characteristics. It is noted that, sequentially, the Fourier coefficients tended to oscillate but in general decreased in magnitude as the mode/frequency increased. In this analysis, the forcing amplitude B was nondimensionalized by the critical forcing amplitude required to achieve lock-in by sinusoidal excitation at the same forcing frequency, $B_{cr,sine}$. The determination of NSR, QP, and LI responses to excitation was made in the same manner as in the experiments, through the inspection of phase portraits and PSD plots. For simplicity, only the critical forcing amplitude B_{cr} required to achieve lock-in is documented here for the various waveforms; additional details may be found in Harris [51].

Table II shows values of the VdP model-determined critical forcing amplitude B_{cr} associated with producing lock-in, normalized by that required for a sinusoidal waveform with the same forcing frequency, $B_{cr,sine}$. The table contains the ratios $B_{cr}/B_{cr,sine}$ for various approximate square waveforms consisting of the first 5, 10, and 15 Fourier terms, with duty cycles α ranging from 10% to 50%, and for the two different forcing frequencies, $f_f = 55$ Hz and 110 Hz. On this basis, values of $B_{cr}/B_{cr,sine}$ that are less than unity indicated that a lower amplitude of excitation would be required for a given waveform to achieve LI as compared with sinusoidal excitation. In all of the forcing cases considered, whether ideal or approximate, the VdP oscillator model showed synchronization for the square wave to require less energy input than required for the sinusoidal waveform (i.e.,

$B_{cr}/B_{cr,sine} < 1$). And while the ideal square waveform required the lowest relative amplitude to achieve LI, the actual square waveforms did provide substantial improvements over sinusoidal excitation requirements, with differences observed for differing numbers of Fourier modes as well as the underlying forcing frequency.

Many, but not all, of the trends observed for the VdP model in Table II directly corresponded to the experimental trends for lock-in described in Table I. For either forcing frequency, $f_f = 55$ Hz or 110 Hz, the ideal square waveform always produced lock-in at a significantly lower forcing amplitude than required for sinusoidal excitation, with B_{cr} amplitudes ranging from 10.9% to 32.3% of the magnitude of $B_{cr,sine}$. For an underlying forcing frequency of 55 Hz, Table II shows that including 10 or 15 Fourier terms in the waveform always improved (reduced) the required amplitude of excitation to achieve LI as compared with 5 terms, consistent with experimental observations noted in Table I for 110 Hz. In fact, for 55 Hz excitation, the VdP model suggested that the required LI amplitudes $B_{cr}/B_{cr,sine}$ were nearly the same for 10 terms as for 15 terms, suggesting that the benefit of the 5 additional terms was negligible beyond 10 Fourier terms. It is also noted that for square-wave forcing at 55 Hz, Fourier terms 4–10 each had frequencies which lay within 50% of the fundamental frequency ($f_o \approx 375$ Hz), with lower magnitude coefficients for terms 11 and above lying beyond the region of the fundamental, similarly suggesting the minimal importance of such terms to the lock-in process. In contrast, for an underlying forcing frequency of $f_f = 110$ Hz, only Fourier terms 2–5 contained frequencies lying within 50% of the fundamental frequency, and as such, one would expect that higher modes (at decreasing magnitudes) would have a lesser influence on achieving lock-in. Indeed, as indicated in Table II for $f_f = 110$ Hz, the minimal forcing amplitude required for LI corresponded to the square wave with 5 terms; beyond this, at 10 or 15 terms, there was a discernible worsening (i.e., an increased required amplitude) the ability to achieve LI. Yet differences between the VdP model-based 110 Hz response in Table II and the trends for the experimental response indicated in I for 110 Hz, where additional Fourier terms improved the ability to achieve lock-in, requires additional scrutiny.

These findings for the simple VdP model at both 55 Hz and 110 Hz square-wave excitation may be interpreted in connection with the typical "lock-in diagram," represented by a plot of the required amplitude for LI as a function of f_f/f_o. As noted by Li and Juniper [42] for the hydrodynamically self-excited jet, a VdP oscillator model typically produces a symmetric V-shaped LI diagram about $f_f/f_o = 1$, suggesting that forcing frequencies equally far from the natural frequency require a larger amplitude to produce lock-in than for f_f values which are closer to f_o. But many flow systems, such as the hydrodynamically self-excited jet, actually produce asymmetric LI diagrams, and the JICF is similarly known to produce an asymmetric V-like shape [41]. For the JICF with sinusoidal axisymmetric excitation, forcing frequencies above the natural frequency require a relatively low amplitude to achieve LI, while for conditions where $f_f < f_o$, very large relative amplitudes are required. This behavior can be used to interpret the present VdP model and experimental observations. As noted above, in square-wave forcing at 55 Hz, there are additional Fourier modes which originate above the fundamental frequency f_o, as compared with the same Fourier terms for the 110 Hz square-wave series. The asymmetry in the LI diagram would suggest, therefore, that the 55 Hz case would more easily achieve lock-in, as observed.

To further explore the significance that specific terms in the Fourier series may influence lock-in, the VdP model was used to explore square-wave excitation at $f_f = 55$ Hz with specific Fourier terms purposely omitted. Table III lists the influence of specific terms on the critical LI amplitude $B_{cr}/B_{cr,sine}$ for α ranging from 10% to 50%; for these cases, the fundamental mode 1 and 8, 9, and 10 were always included, but the additional (second) mode was varied. The results in Table III suggest that for duty cycles of 20%, 30%, and 40%, the first listed case, with Fourier mode 2 included, required the least energy input to achieve LI, while for duty cycles of 10% and 50%, the last case listed, with Fourier mode 5 included, was optimal in achieving LI. The Fourier coefficients themselves were dependent in these waveforms on the duty cycle as well as the frequency, and in all cases indicated here, the Fourier coefficients producing optimal lock-in generally had the largest magnitudes (beyond the coefficient amplitude for mode 1). Hence, both the amplitude of the

TABLE III. Tabulation of the normalized critical forcing amplitude $B_{cr}/B_{cr,sine}$ for synchronization of the VdP oscillator model to square-wave forcing at $f_f = 55\,\text{Hz}$, with 5 selected terms from the Fourier series. Waveforms were generated for duty cycles α ranging from 10% to 50%.

5-term Fourier series	$\alpha = 10\%$	$\alpha = 20\%$	$\alpha = 30\%$	$\alpha = 40\%$	$\alpha = 50\%$
Terms 1, 2, 8, 9, 10	0.655	0.588	0.664	0.706	0.807
Terms 1, 3, 8, 9, 10	0.613	0.664	0.697	0.790	0.790
Terms 1, 4, 8, 9, 10	0.597	0.597	0.681	0.756	0.806
Terms 1, 5, 8, 9, 10	0.546	0.697	0.689	0.798	0.681

Fourier coefficients and the proximity of the mode to the natural frequency contributed to the ability to achieve dynamical lock-in for the JICF.

These findings can also help to explain the imperfect square waveforms created by the Fourier series in the present methodology, e.g., as shown in Fig. 3. Figure 6 shows the resulting waveforms produced for $f_f = 55$ Hz and $\alpha = 30\%$ by the four alternative cases shown in Table III, with the associated "R-squared" value representing the goodness of fit to the actual square waveform. As expected from Table III, the case in Fig. 3(a) produced the best fit (quantitatively) to the square wave, though in all cases there was a substantial degree of ringing in the waveforms, not unlike those seen in the experiments. Thus, clearly the mathematical form of the temporal axisymmetric excitation not only affects the waveform's accuracy, but also the dynamical response and lock-in of the jet, with attendant implications for structural alterations and mixing.

B. Vorticity evolution and jet dynamics

1. Vorticity and structure

The effects of various kinds of axisymmetric excitation on jet structure, vorticity generation and evolution, and molecular mixing are of great interest here, given the various practical applications of the JICF. Prior experiments with square-wave excitation of the transverse jet [37], utilizing acetone PLIF imaging, demonstrate a significant influence on the JICF with a naturally AU USL, where deeply penetrating, periodic vortices with improved jet penetration and spread can take place. Yet it is found that enhanced jet penetration does not always correlate with better molecular mixing of jet and crossflow. For example, it is documented [37], especially at higher J values, that there is a stronger correlation of improved mixing with creation of a more symmetric jet cross section than with a less symmetric structure without a clear CVP structure. More recent studies by Harris *et al.* [39] demonstrate similar findings for a double-pulse forcing waveform, though with additional insights because of the ability to control vortex formation, collision, and avoidance in a systematic manner. When the JICF is absolutely unstable, for example, the greatest enhancement in mixing occurs when the vortex rings do not interact. Yet these prior studies did not explore velocity or vorticity fields via stereo PIV simultaneous to the PLIF imaging, and hence the present studies offer insights not only into the relationship between jet vorticity and scalar structure and mixing, but perhaps more importantly, how differing states of synchronization to the applied forcing can affect dynamics in the nearfield of the jet, such as those associated with the vortex rollup along the jet USL, and ultimately affect the formation, strength, and symmetry of the CVP further downstream.

The effect of the state of synchronization of the jet to the applied excitation may be explored here, for JICF responses classified as in Table I. In most cases here we fixed the waveform and altered the excitation amplitude and other flow parameters. While many cases are documented in Harris [51], here we focus on the $f_f = 110\,Hz$ sinusoidal waveform and the 0.35.65.80 double-pulse waveform, both listed in Table I. In our prior study on double-pulse excitation [39], a similar waveform to 0.35.65.80 produced sequential vortical structures that slightly interacted with one another but did

(a) $R^2 = 86\%$

(b) $R^2 = 63\%$

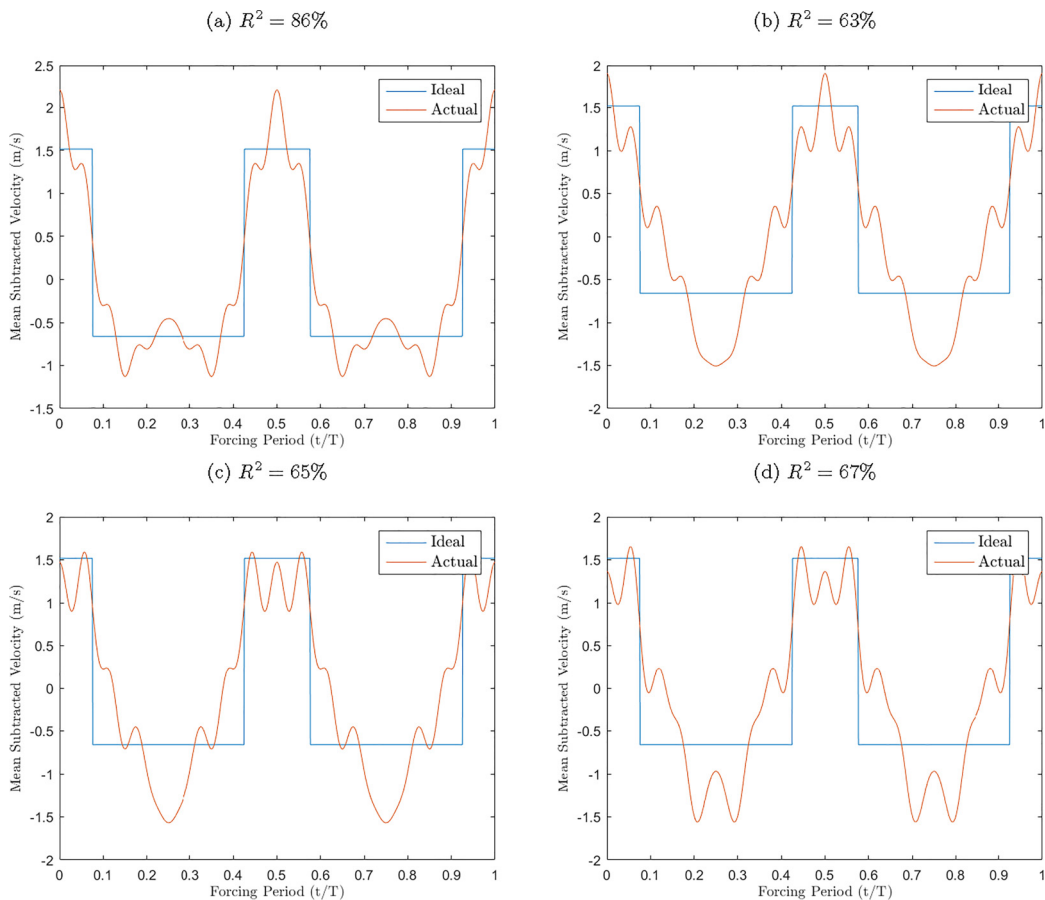(c) $R^2 = 65\%$

(d) $R^2 = 67\%$

FIG. 6. Waveforms created by approximate square-wave excitation at $f_f = 55$ Hz and duty cycle $\alpha = 30\%$ with 5 selected terms from the Fourier series (red), with comparison to the ideal square waveform (blue). Shown are mean-subtracted velocity temporal evolution for: (a) terms 1, 2, 8, 9, and 10 with an R-squared of 86%, (b) terms 1, 3, 8, 9, and 10 with an R-squared of 63%, (c) terms 1, 4, 8, 9, and 10 with an R-squared of 65%, and (d) terms 1, 5, 8, 9, and 10 with an R-squared of 67%. For accurate comparison the mean and RMS of the waveforms were matched.

not fully collide when the jet's velocity perturbation was relatively high, $u'_{j,\mathrm{rms}}/U_j \approx 0.6$, and tended to have in general very good molecular mixing. In contrast, sinusoidal excitation for a naturally AU transverse jet has been found in prior studies under similar conditions to typically mix less well than for square-wave excitation [37].

To visualize the flow, stereo-PIV was used for imaging in the jet centerplane, and at several nearfield cross-sectional slices of the jet. Additionally, further downstream, at cross-sectional locations of $x/D = 1.5$, $x/D = 2.5$, and $x/D = 5.5$, acetone PLIF imaging was used to document the structural evolution of the jet. The flow conditions for the jet corresponded to several cases in Table I, where excitation was applied at increasing nondimensional forcing amplitudes ranging from $u'_{j,\mathrm{rms}}/U_j = 0.0$ (unforced jet) to 0.50 (well above LI). Figures 7 and 8 present the mean vorticity field extracted from stereo PIV in the centerplane and at cross-sectional locations corresponding to $x/D = 0.0$ and $x/D = 1.0$, along with the mean cross-sectional structure from PLIF imaging at $x/D = 5.5$, for the 0.35.65.80 double-pulse waveform and the $f_f = 110\,Hz$ sinusoidal waveform, respectively. Here the images were averaged over 600 instantaneous realizations, and the colorbars were individually scaled to the maximum and minimum values contained within each mean image.
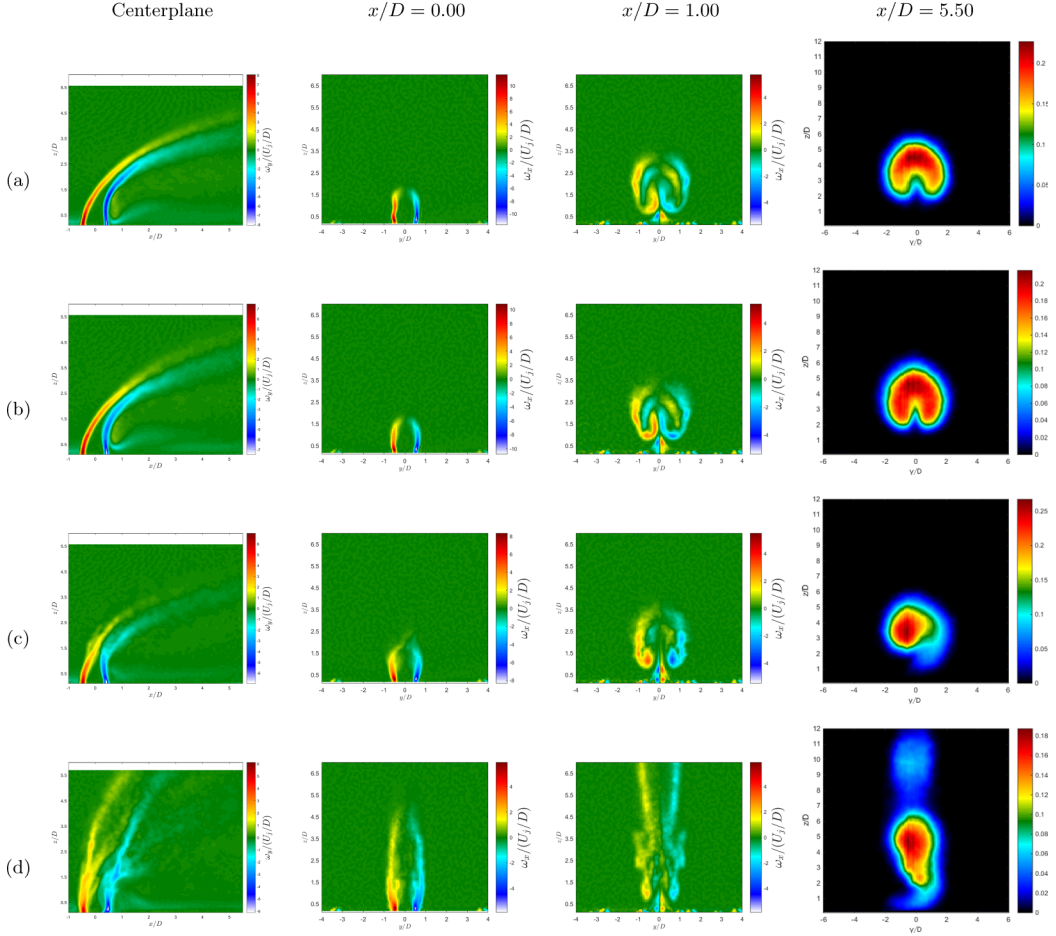
FIG. 7. Mean vorticity along the jet centerplane, mean vorticity at jet cross-sectional locations $x/D = 0.0$ and $x/D = 1.0$, and mean cross-sectional jet scalar concentration at $x/D = 5.5$ for axisymmetric excitation corresponding to the 0.35.65.80 double-pulse waveform. Excitation amplitudes and synchronization responses include: (a) $u'_{j,\mathrm{rms}}/U_j = 0.00$ (unforced), (b) $u'_{j,\mathrm{rms}}/U_j = 0.02$ (barely LI), (c) $u'_{j,\mathrm{rms}}/U_j = 0.16$ (LI), and (d) $u'_{j,\mathrm{rms}}/U_j = 0.50$ (well above LI).

The unforced jet mean vorticity and scalar field images in Figs. 7(a) and 8(a) depict relatively symmetric cross-sectional vorticity fields in the vicinity of the jet exit, as well as a clearly symmetric CVP structure in the jet cross-section, consistent with an absolutely unstable JICF observed in prior experiments [20]. For an applied forcing of $u'_{j,\mathrm{rms}}/U_j = 0.02$, the double square-waveform excitation was found in Table I to produce lock-in of the upstream shear layer, while for sinusoidal excitation, there was less of a response, producing quasiperiodicity in the USL. Interestingly, this (barely) LI response for the double square wave manifested in slight alterations in the cross-sectional vorticity and a slight broadening of the still-symmetric CVP structure in Fig. 7(b), though for the QP response to sinusoidal excitation, there were negligible alterations in the jet's mean vorticity and scalar field, even in the cross-sectional views, shown in Fig. 8(b). Further increasing the forcing ampltude beyond that which was needed for LI for either waveform, to $u'_{j,\mathrm{rms}}/U_j = 0.16$, resulted in the apparent elimination of the CVP for each case, according to the jet structure at $x/D = 5.5$ in Figs. 7(c) and 8(c). From the mean vorticity along the upstream and downstream shear layers in the centerplane views, it appeared the leading and trailing edges of the vortex rings interacted
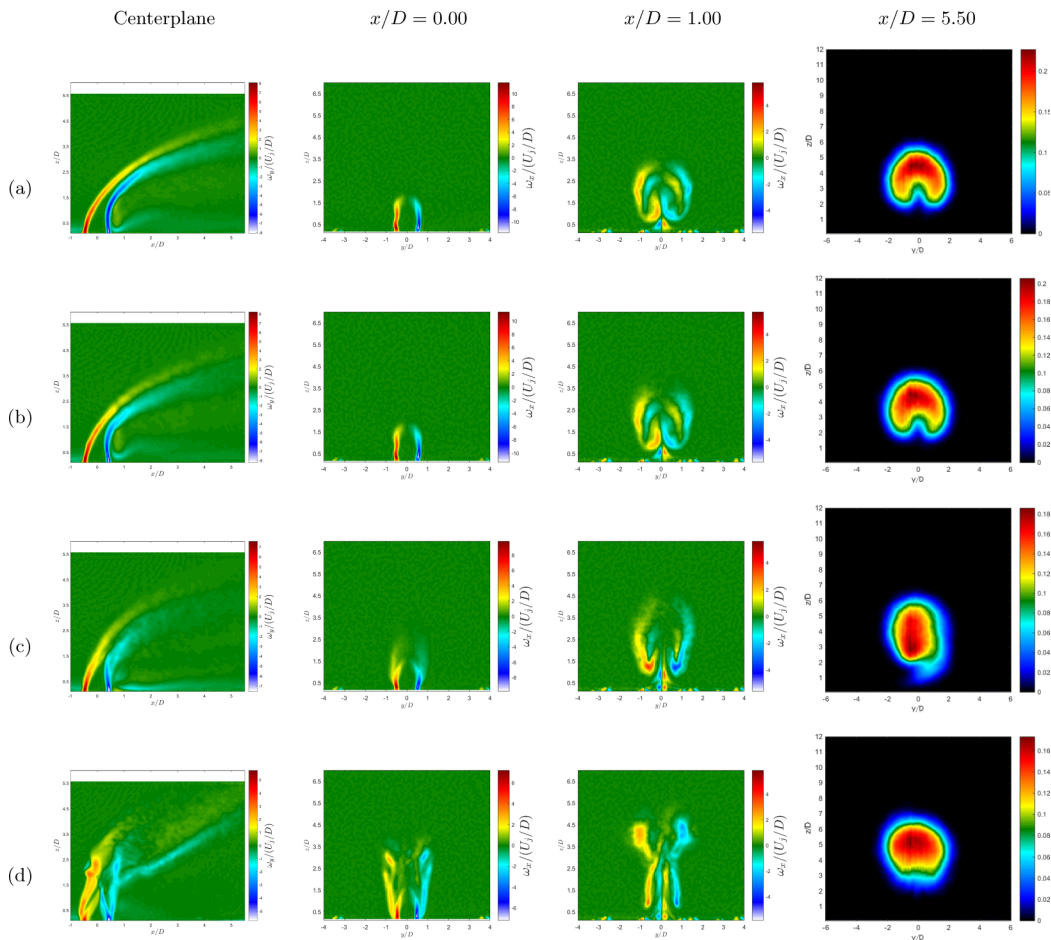
FIG. 8. Mean vorticity along the jet centerplane, mean vorticity at jet cross-sectional locations $x/D = 0.0$ and $x/D = 1.0$, and mean cross-sectional jet scalar concentration at $x/D = 5.5$ for axisymmetric excitation corresponding to the sinusoidal waveform at $f_f = 110 Hz$. Excitation amplitudes and synchronization responses include: (a) $u'_{j,\mathrm{rms}}/U_j = 0.00$ (unforced), (b) $u'_{j,\mathrm{rms}}/U_j = 0.02$ (QP), (c) $u'_{j,\mathrm{rms}}/U_j = 0.16$ (LI), and (d) $u'_{j,\mathrm{rms}}/U_j = 0.50$ (well into LI).

sooner and broke down in the nearfield of the jet for the double-pulse waveform. There was a lesser degree of such interactions in the sinusoidal case, but for sine wave perturbations, a slight increase in jet penetration was apparent. The cross-sectional mean vorticity and scalar fields for sinusoidal excitation in Fig. 8(c) similarly showed a broadening in the vertical (z) direction as compared with double-pulse square excitation and the unforced conditions in Figs. 7(c) and 7(a), respectively. This was somewhat unexpected given the numerous studies which note square-wave excitation of an AU jet produces more distinctive alterations and increased mean jet penetration as compared with the effects of sine wave excitation [32,36], though acetone PLIF imaging demonstrated that for many specific conditions, sinusoidal excitation could improve both penetration and mixing over certain square-wave excitation cases when perturbation amplitude is matched [37]. In the present studies, when the forcing amplitude was raised well above the LI threshold for these waveforms, to $u'_{j,\mathrm{rms}}/U_j = 0.50$, the vorticity and scalar fields as shown in Figs. 7(d) and 8(d) showed more significant differences. Fig. 7(d) shows a much greater degree of jet penetration for the double-pulsed excitation, both in the centerplane view as well as the cross-sectional mean vorticity

in the nearfield and and the mean scalar field cross-section further downstream, than for comparable images for sinusoidal excitation in Fig. 8(d). For both cases there were bifurcated jet structures visible in the centerplane, but for sinusoidal excitation a lee-side flow structure resembling a tertiary vortical structure could be initiated, as shown, but with relatively symmetric cross-sectional shapes without the typical CVP structure. Such differences were generally consistent with other excitation amplitudes well above conditions producing lock-in, though some differences could be explored more effectively by examining altered dynamical characteristics via image analysis.

2. POD analysis and phase reconstruction

To explore the underlying structure, dynamics, and dominant instabilities of the flowfield in greater detail from instantaneous imaging of the flow, snapshot proper orthogonal decomposition (POD) [57] was applied to the velocity vector fields extracted from the centerplane stereo-PIV imaging. This technique has been utilized in other studies of the JICF [23,58], including those in the present facility for the unforced JICF [28] and the JICF with passive tabs [30] as well as asymmetric excitation [52]. In the present study, snapshot POD analysis was applied to 600 instantaneous realizations of the flowfield for each test case considered, well above the 300 snapshots required for statistical convergence [44]. Further still, in cases where the flow was synchronized to the applied forcing, the imaging rate was such that pseudo time-resolved data were acquired with approximately 135 images per single forcing period, providing a relatively well-refined examination of the flow. The resolved mode structures were ordered in terms of their respective magnitudes of total kinetic energy (TKE) fluctuation, helping to reveal characteristic flow features and dynamics which might otherwise be hidden or masked by the seemingly chaotic flowfield.

Figures 9(a)–9(c) provide examples of POD modal analysis results, depicting the three most energetic mode structures for the transverse jet under unforced conditions, with the 0.35.65.80 double-pulse excitation, and with sinusoidal excitation, respectively. For each case with forcing, the excitation amplitude, $u'_{j,\mathrm{rms}}/U_j = 0.41$, produced conditions that were well into lock-in conditions per Table I. Shown for each of the POD modal shapes are their respective contributions to the total kinetic energy fluctuation. While there were striking visual differences in the POD mode plots for each case, e.g., with a significant increase in jet vertical spread and in development of finer wake structures for mode 3 in the double-pulse excitation case as compared with the unforced case or for sinusoidal forcing, the differences in the energetic content were even more striking. Energetic content for the unforced JICF in Fig. 9(a) was much lower for modes 1 and 2, in particular, than for the double-pulse excitation case in Fig. 9(b), and was significantly lower than for sinusoidal excitation in in Fig. 9(c). The double-pulse square wave's multiple modes (i.e., the fundamental forcing frequency and 14 higher modes creating the waveform) and associated distribution of modal energy, in contrast to the single applied frequency for sinusoidal excitation, likely explains this difference in energetic content. This observation was repeated for many other cases comparing POD modal TKE content for double-pulse square wave to sinusoidal excitation at strong lock-in conditions, suggesting that over 50% of the sinusoidally excited jet's dynamical energetic content could be captured using just two POD modes, while many more modes would be required to characterize the energetic dynamics of the JICF exposed to double-pulse square wave or other complex excitation waveform.

Understanding the dynamical character of JICF response via the POD analysis may be extended by examining correlations in the evolution of these mode dynamics across the series of original snapshots. For a specific snapshot image, the value of each POD mode coefficient represented the contribution of that particular mode in the reconstruction of the original snapshot from all of the modes. By plotting the mode coefficients of the first two or three most dominant modes against one another, for each of the individual snapshots, a phase portrait could be generated depicting the coupling, or lack thereof, of the mode dynamics in the phase space. This approach has been utilized in other studies of the JICF, as noted above, for two [23,28,30,58] and three POD mode coefficients [52]. In the present study, 3D phase portraits for the sample POD modes in Fig. 9 are
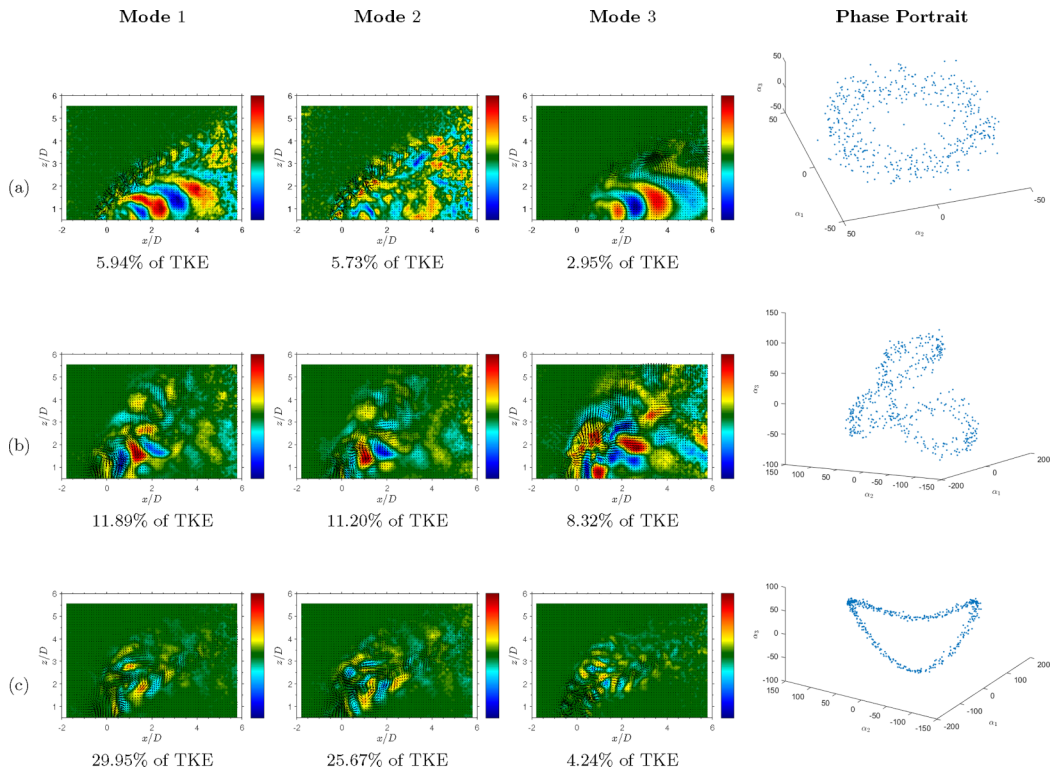
FIG. 9. PIV-based POD mode structures (modes 1-3) as well as the associated 3D mode coefficient plots (phase portraits): (a) unforced conditions, (b) 0.35.65.80 double-pulse waveform excitation, and (c) sinusoidal excitation at $f_f = 110$ Hz, the latter two with amplitude $u'_{j,\mathrm{rms}}/U_j = 0.41$. Shown for each mode is its relative percentage of total kinetic energy fluctuation content. The colorbar in each image represents the mode scaled by its own norm and the mean jet velocity at the jet exit, U_j.

shown in the last column, for the unforced case (a) and for each forced waveform, double-pulse in (b) and sinusoidal in (c), at relative amplitude $u'_{j,\mathrm{rms}}/U_j = 0.41$. The typical roughly circular structure in the mode coefficient plot appeared for the naturally AU unforced jet in Fig. 9(a), as expected, with the ringlike trajectory of points representative of a limit cycle attractor and hence representing a periodic traveling wave [28,58]. For sinusoidal excitation in Fig. 9(c) there was a relatively simple, though slightly deflected circular periodic structure, whereas in double-pulse excitation [Fig. 9(b)] there were multiple intersecting loops in the dynamical characterization.

More extensive results for both the sinusoidal and double-pulse forcing are shown in Fig. 10, including additional forcing amplitudes considered for both waveforms, corresponding to the cases documented in Figs. 7 and 8. At the relatively low amplitude forcing with $u'_{j,\mathrm{rms}}/U_j = 0.02$, in Fig. 10(a), while double-pulse square-wave excitation resulted in QP in the upstream shear layer, and sinusoidal excitation had barely achieved LI, per Table I, the phase portraits were barely differentiable from that for the unfoced case in Fig. 9(a). This observation was consistent with the resulting vorticity and scalar field images for these cases in Figs. 7 and 8. Stronger axisymmetric excitation of the jet at $u'_{j,\mathrm{rms}}/U_j = 0.16$ corresponded to LI for both excitation conditions shown in Fig. 10(b), and while the single loop, ringlike trajectory for sinusoidal excitation remained, double-pulse excitation produced an additional loop, reflecting the two distinct vortex rings which were generated during each forcing period. This additional complexity in the phase portraits for the double-pulse excitation continued at higher amplitude forcing, as compared with sine wave forcing, seen for amplitude $u'_{j,\mathrm{rms}}/U_j = 0.41$ in the last column in Figs. 9(b) and 9(c), and for $u'_{j,\mathrm{rms}}/U_j = 0.50$ shown in
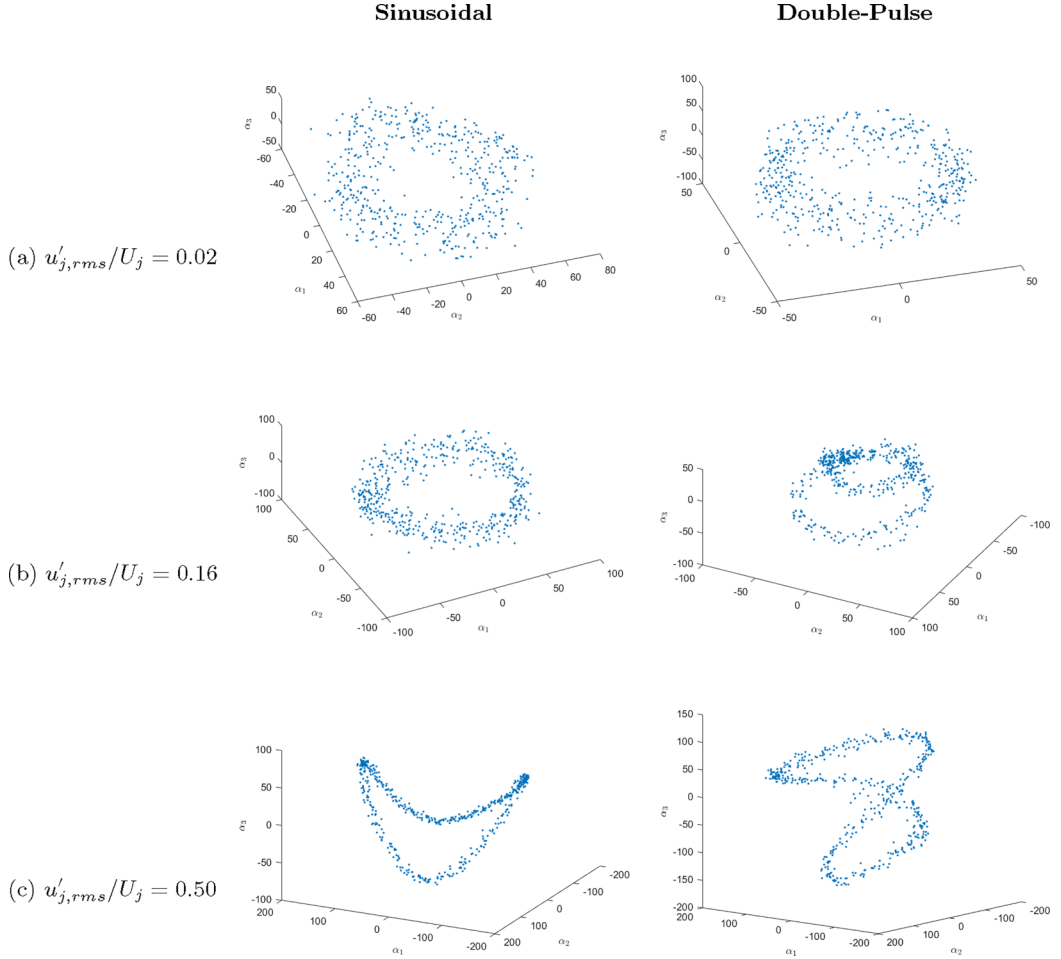
Sinusoidal **Double-Pulse**

FIG. 10. PIV-based POD coefficients of the first three modes plotted against one other, for the $f_f = 110\,\mathrm{Hz}$ sinusoidal (left) and 0.35.65.80 double-pulse (right) waveforms, with the following amplitudes: (a) $u'_{j,\mathrm{rms}}/U_j = 0.02$, (b) $u'_{j,\mathrm{rms}}/U_j = 0.16$, and (c) $u'_{j,\mathrm{rms}}/U_j = 0.50$.

Fig. 10(c). Here, under conditions well into LI, the double-pulse waveform continued to produce a double-loop phase trajectory, while the sinusoidal waveform continued to produce a simple though slightly distorted single-loop trajectory, both of which increased in coherence with the increasing forcing amplitude.

Among the interesting findings from the separate high resolution PLIF-only experiments for double-pulse JICF excitation studies in Harris *et al.* [39] is that when the jet is naturally CU, forcing which promotes vortex collisions provides the greatest enhancement in molecular mixing, while the AU jet produces the greatest enhancement in mixing when collisions do not occur and the vortex rings do not interact. The present study's focus on the dynamical character of this flowfield can help to interpret these and related observations. It was thus of interest to select a succession of waveforms with matched amplitudes of excitation but where the spacing of the pulses and hence the degree of vortex interactions could be altered.

In the present tests, a high amplitude excitation condition, $u'_{j,\mathrm{rms}}/U_j = 0.50$, was applied to a succession of waveforms with the same temporal pulse-widths of the slow and fast pulses, $\tau_1/T = 0.35$ and $\tau_2/T = 0.15$, but where the temporal spacing between the two pulses was systematically
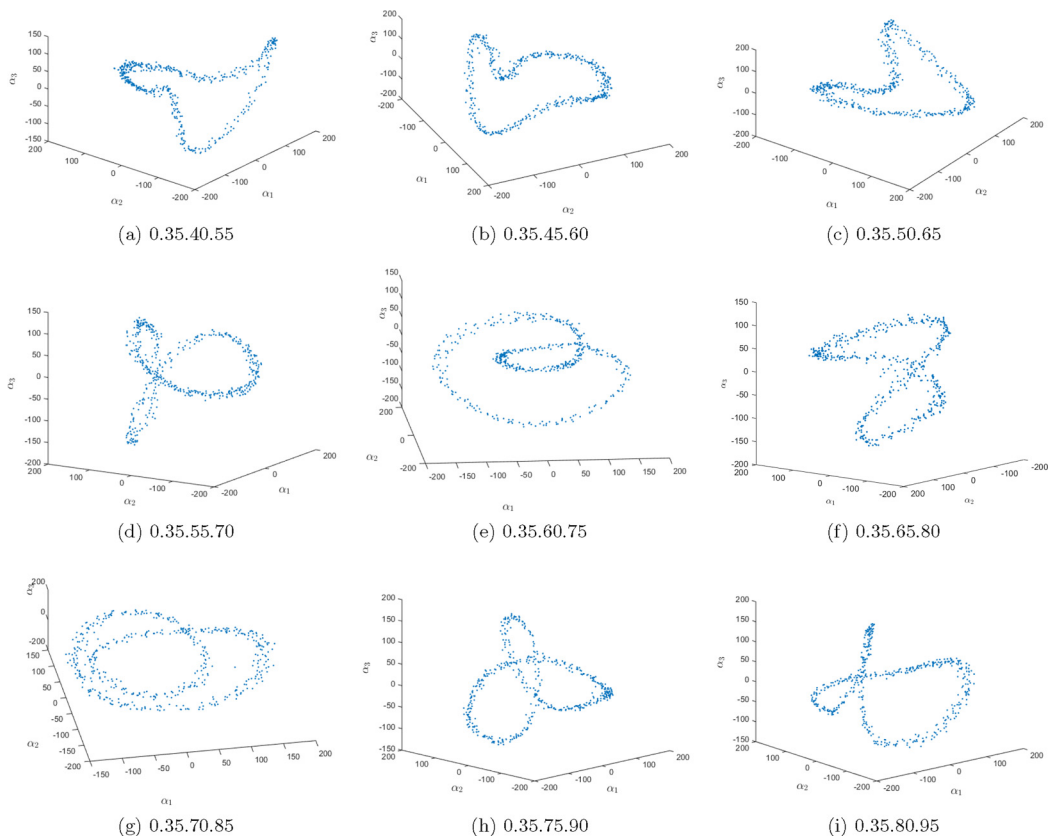
FIG. 11. PIV-based POD coefficients of the first 3 modes plotted against each other. For these cases, the forcing amplitude of $u'_{j,\mathrm{rms}}/U_j = 0.50$ was matched and the temporal pulse-width of the slow and quick pulses were fixed at $\tau_1/T = 0.35$ and $\tau_2/T = 0.15$, respectively, while the temporal spacing between slow and fast pulses was varied in increments of $t/T = 0.05$.

increased, from $\Delta\tau_{1\rightarrow2}/T = 0.05$ to $\Delta\tau_{2\rightarrow1}/T = 0.05$, in increments of $t/T = 0.05$. Figure 11(a)–11(j) show the mode coefficient phase portraits composed from the first 3 most dominant POD modes for each forcing waveform. Figure 11(a), for example, corresponds to waveform 0.35.40.55, where temporally the fast pulse was issued from the jet exit at a value of $\Delta\tau_{1\rightarrow2}/T = 0.05$ in time after the slow pulse. For this particular case, the phase portrait lacked the distinct double-loop trajectory which had been noted in Fig. 10(b) for the 0.35.65.80 double-pulse forcing. As the temporal spacing between the slow and fast pulses was gradually increased, in Figs. 11(b) and 11(c), the trajectory remained as a single loop, but with increasing distortion, until multiple loops in the phase portrait were formed, beginning in Fig. 11(d) for the double-pulse waveform 0.35.55.70, in which the quick pulse followed the slow in time at $\Delta\tau_{1\rightarrow2}/T = 0.20$. As the temporal spacing between slow and fast pulses continued to increase incrementally for the fixed overall period (or frequency), in Figs. 11(e)–11(i), the multiple loops became more clearly visible, though with altered topology, consistent with differing degrees of vortex interactions and timescales. There was a slight alteration in the multiple loop phase portrait in Fig. 11(j), with the waveform 0.35.80.95, where the quick pulse was issued $\Delta\tau_{1\rightarrow2}/T = 0.45$ temporally after the slow pulse, and as a result the subsequent slow pulse from the following forcing period issued only $\Delta\tau_{2\rightarrow1}/T = 0.05$ temporally after the quick pulse. For this case the double loop topology began to disappear, returning to the original type of waveform in Fig. 11(a) for the given constraints. From these trends in the trajectory

(a) Center of jet exit

(b) $s/D = 0.5$

(c) $s/D = 1.0$

(d) $s/D = 1.2$
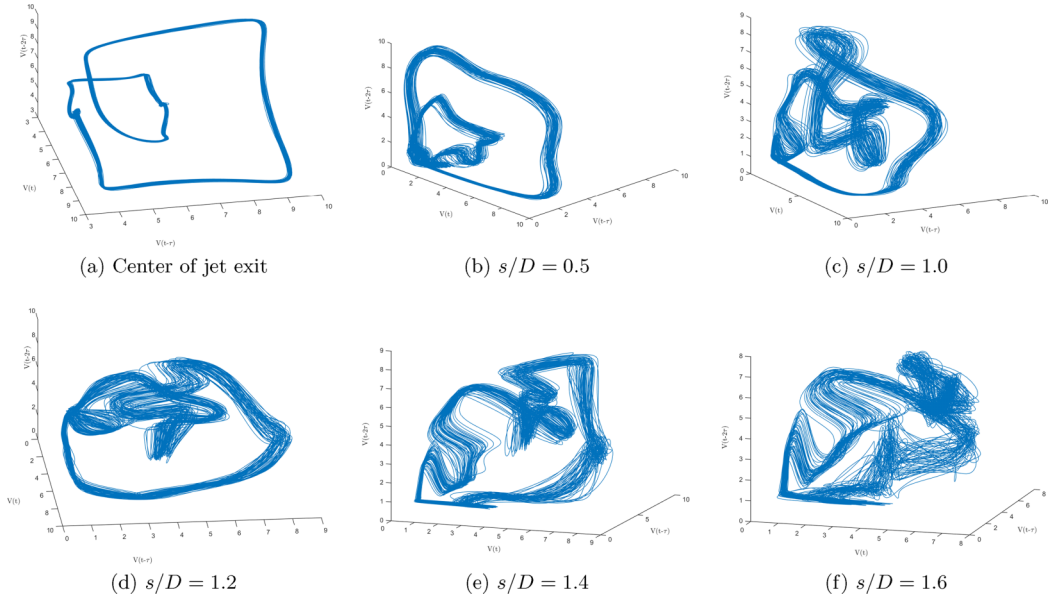
(e) $s/D = 1.4$

(f) $s/D = 1.6$

FIG. 12. Phase portraits from time delay embedding of the hotwire-based vertical velocity fluctuations along the USL of the jet for the 0.35.45.60 double-pulse waveform with amplitude $u'_{j,\mathrm{rms}}/U_j = 0.50$. Shown are data extracted from: (a) the center of the jet just above the nozzle exit plane, and (b–f) at locations along the USL indicated by s/D values. The corresponding PIV-based POD mode coefficient plot for the entire FOV is shown in Fig. 11(b).

shape, it appeared that the temporal spacing between the termination of the slow pulse and the emergence of the quick pulse, $\Delta\tau_{1\to2}/T$, was much more significant in controlling the onset of the double-loop trajectory as compared with the temporal spacing between the termination of the quick pulse and the emergence of the slow pulse, $\Delta\tau_{2\to1}/T$.

The 3D phase space reconstructions from the POD mode coefficients shown in Figs. 10 and 11 represent the dynamics contained within the entire field of view extracted from snapshot PIV images, spanning nearly six diameters into the downstream wake region of the jet. Yet given that hotwire-based measurements of vertical velocity fluctuations along the upstream shear layer have been used extensively in characterization of the jet dynamics, including in the present paper in Fig. 5, it was of interest to compare phase portraits generated from hotwire measurements at different USL locations with the PIV-based POD phase portraits in Fig. 11, where the former were based on time-delay embedding, as described previously. Figures 12–14 show hotwire-based phase portraits for the double pulse excitation cases designated by 0.35.45.60, 0.35.55.70, and 0.35.75.90, respectively, at the center of the jet just above the exit plane and at a number of USL locations ranging from $s/D = 0.5$ to 1.6.

In all excitation cases in Figs. 12–14, the vertical velocity fluctuations of the forced jet at the center of the exit plane were represented by a clear double-loop phase space trajectory, consistent with double-pulse excitation and formation of two vortex rings during a single forcing period. The persistence of this double-loop phase trajectory along the jet's upstream shear layer was found to be dependent on the temporal spacing between the slow and quick pulses of the waveform, similar to that observed in PIV-based POD phase portraits for the entire FOV. For example, in Fig. 12, for the 0.35.45.60 waveform, after initiation of the secondary loop at the exit plane, as one transitions along the USL in Figs. 12(b)–12(e), there was a fairly rapid deterioration of the secondary loop. This degradation of the secondary loop was associated with the quick pulse's interacting with the slow pulse in the jet nearfield, promoting vortex merger and breakdown. Beyond the location
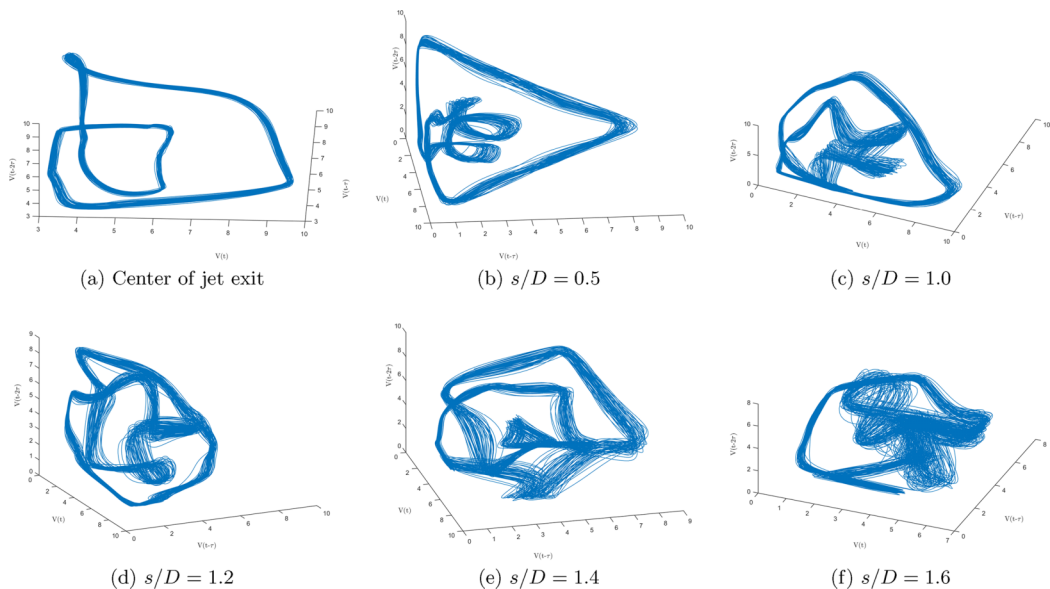
FIG. 13. Phase portraits from time delay embedding of the hotwire-based vertical velocity fluctuations along the USL of the jet for the 0.35.55.70 double-pulse waveform with amplitude $u'_{j,\mathrm{rms}}/U_j = 0.50$. Shown are data extracted from: (a) the center of the jet just above the nozzle exit plane, and (b–f) at locations along the USL indicated by s/D values. The corresponding PIV-based POD mode coefficient plot for the entire FOV is shown in Fig. 11(d).

$s/D = 1.4$, for example, at $s/D = 1.6$ in Fig. 12(f) and further along the shear layer (not shown), the secondary loop was less distinguishable and eventually transitioned to a chaotic blob with no coherent trajectory at all, at least in part due to an altered (bifurcated) jet trajectory attempting to be captured with a single hotwire probe. The corresponding PIV-based POD phase portrait for the entire FOV, shown in Fig. 11(b), showed an absence of a secondary loop for this excitation case, phenomenologically consistent with the evolution in the local hotwire-quantified dynamics.

In cases where the vortical pulses did not interact as significantly, as in the double-pulse waveforms 0.35.55.70 and 0.35.75.90, their hotwire-based phase portraits in Figs. 13 and 14, respectively, showed a persistence in the secondary loop initiated at the jet exit, in both cases to an upstream shear layer location of at least $s/D = 1.4$, and possibly to $s/D = 1.6$. The secondary loop structure(s) were consistent with the PIV-based POD mode coefficient plots for these cases shown in Figs. 11(d) and 11(i). Hence, one might consider the single vs. double loop structures in the phase portraits to act as a kind of characteristic signature for the degree of interaction of the vortical structures created by such double-pulse excitation.

C. Molecular mixing

Given the correspondence of the degree of vortical interactions to the dynamics of the JICF, as documented in the differing phase portrait signatures shown in Sec. III B 2 and different vorticity fields in Sec. III B 1, it was of interest to study the degree of molecular mixing quantified for jets excited under these specific conditions. As in our prior studies [37–39], the molecular mixing was quantified based on the instantaneous unmixedness parameter, which was determined from scalar PLIF images taken simultaneously to the PIV in the jet centerplane. Calculating the unmixedness, which represents the second moment of the scalar concentration field, was obtained using Eq. (4), where lower values of unmixedness correspond to better molecular mixing. For each of these
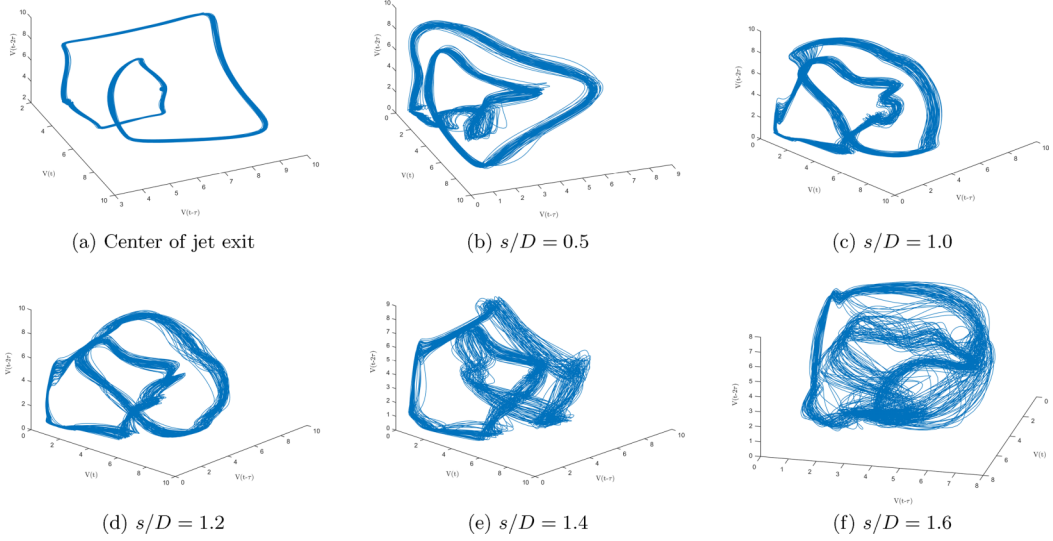
FIG. 14. Phase portraits from time delay embedding of the hotwire-based vertical velocity fluctuations along the USL of the jet for the 0.35.75.90 double-pulse waveform with amplitude $u'_{j,\mathrm{rms}}/U_j = 0.50$. Shown are data extracted from: (a) the center of the jet just above the nozzle exit plane, and (b–f) at locations along the USL indicated by s/D values. The corresponding PIV-based POD mode coefficient plot for the entire FOV is shown in Fig. 11(i).

evaluations in the flowfield, the validity became unreliable after approximately $x/D = 5.5$ because certain jet forcing cases were found to propagate out of the FOV captured in the PLIF images.

Figure 15 presents the centerplane-based molecular mixing quantifications of the JICF when excited by the $f_f = 110\,\mathrm{Hz}$ sinusoidal and 0.35.65.80 double pulse waveforms investigated in Secs. III A 1 and III B 1, for forcing amplitudes corresponding to synchronization states of QP, LI and well beyond LI. In all cases, along the jet trajectory itself, as was typical in prior studies, the jet mixing improved as increased mass exchange between jet and crossflow took place. Consistent with the vorticity, jet structure, POD modes shapes, and POD-based phase portraits, the sinusoidal and double-pulse forcing at $u'_{j,\mathrm{rms}}/U_j = 0.02$ resulted in mixing characteristics which were qualitatively and quantitatively nearly the same as the unforced jet, verifying that dynamical responses of QP or barely LI for the upstream shear layer produced little benefit in terms of mixing. At successively higher amplitude excitation, however ($u'_{j,\mathrm{rms}}/U_j = 0.16$, 0.41, and 0.50), the unmixedness was successively reduced for each of the waveforms, implying successive improvement in molecular mixing. But in some cases, at a fixed amplitude, sinusoidal excitation produced better overall mixing (e.g., for $u'_{j,\mathrm{rms}}/U_j = 0.16$ and 0.50), but in the case of $u'_{j,\mathrm{rms}}/U_j = 0.41$, the double-pulse square excitation had improved mixing further downstream. It should be noted, however, that the structure of the jet played a role in this mixing quantification. For the case with $u'_{j,\mathrm{rms}}/U_j = 0.41$, the increased strength of the double-pulse forcing acted to increase the degree of bifurcation of the jet, and as a result presumably affected the nearfield vortex interactions, vortex breakdown, and hence nearfield molecular mixing. So while the state of the USL (e.g., being well into lock-in) was effective in predicting improved mixing, this was not the only condition of importance in optimizing transverse jet behavior.

In an effort to systematically determine which type of forcing waveform could be optimal in altering the dynamics as well as the mixing characteristics for the JICF, sinusoidal forcing was compared with various types of square-wave and double-pulse forcing waveforms, all at the same forcing frequency of $f_f = 110\,\mathrm{Hz}$ and with a matched forcing amplitude of $u'_{j,\mathrm{rms}}/U_j = 0.50$. As determined previously, sinusoidal forcing applied at $f_f = 110\,\mathrm{Hz}$ locked-in the jet shear layer
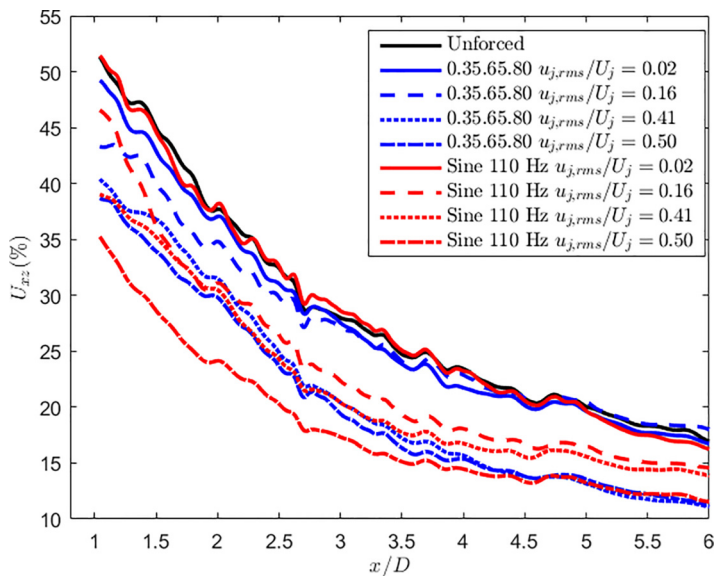
FIG. 15. Evolution of centerplane unmixedness, U_{xz}, comparing the response of the jet to $f_f = 110$ Hz sinusoidal excitation (red) and 0.35.65.80 double-pulse excitation (blue) at forcing amplitudes ranging from $u'_{j,\mathrm{rms}}/U_j = 0.02$ to $u'_{j,\mathrm{rms}}/U_j = 0.50$, in addition to unforced conditions (black solid line).

much more easily than sinusoidal forcing at the same amplitude but at frequency $f_f = 55$ Hz due to the greater proximity of the former's forcing frequency to the fundamental, $f_o \approx 357$ Hz. Figure 16 presents a comparison of molecular mixing in the centerplane for experiments with a number of alternative waveforms. For square-wave excitation with alternative duty cycles α, Fig. 16(a) shows that all of the square waveforms improved molecular mixing between jet and crossflow fluid, but the best mixer, producing the lowest unmixedness, was the square wave with a 40% duty cycle. As documented in Shoji *et al.* [37], Harris *et al.* [39], the $\alpha = 40\%$ square wave was associated with the formation of vortex structures with fully filled rings, without the presence of a trailing column of jet fluid, which typically would produce improved mixing as compared with smaller duty cycles (with weak vortex rings) or larger duty cycles (with trailing columns), each of which produced a lesser degree of mixing. This vortex ring relationship to mixing was also consistent with theoretical predictions of vortex ring entrainment by Sau and Mahesh [35].

Double-pulse square-wave excitation in Figs. 16(b) and 16(c) compared waveforms where the temporal spacing between the quick and slow pulses was varied while maintaining the temporal pulse-widths of each of the two distinct pulses, to explore the influence of the vortex interactions and associated phase portraits documented in the prior section. Figure 16(b) compared the double-pulse waveforms with slow and quick temporal pulse-widths of $\tau_1/T = 0.35$ and $\tau_2/T = 0.15$ respectively. The best molecular mixer (lowest continual unmixedness evolving downstream) was found to correspond to waveform 0.35.45.60, though others with relatively close spacing of the pulses (0.35.40.55 and 0.35.50.65) were also among the better mixers. Dynamically, the 0.35.45.60 case corresponded to the waveform that eliminated the double-loop trajectory in the phase space most rapidly (Fig. 11), and as noted earlier, was representative of significant nearfield interactions and breakdown of the vortex rings. In contrast, forcing cases producing more complex, multiloop phase portraits in Fig. 11, e.g., 0.35.60.75, produced molecular mixing that was not significantly better than that for the unforced jet. Hence, in this case the excitation producing simpler dynamics and single loop trajectories corresponded to improve molecular mixing. Figure 16(c) shows the evolution of molecular mixing for double-pulse excitation with a broadened temporal pulse-width
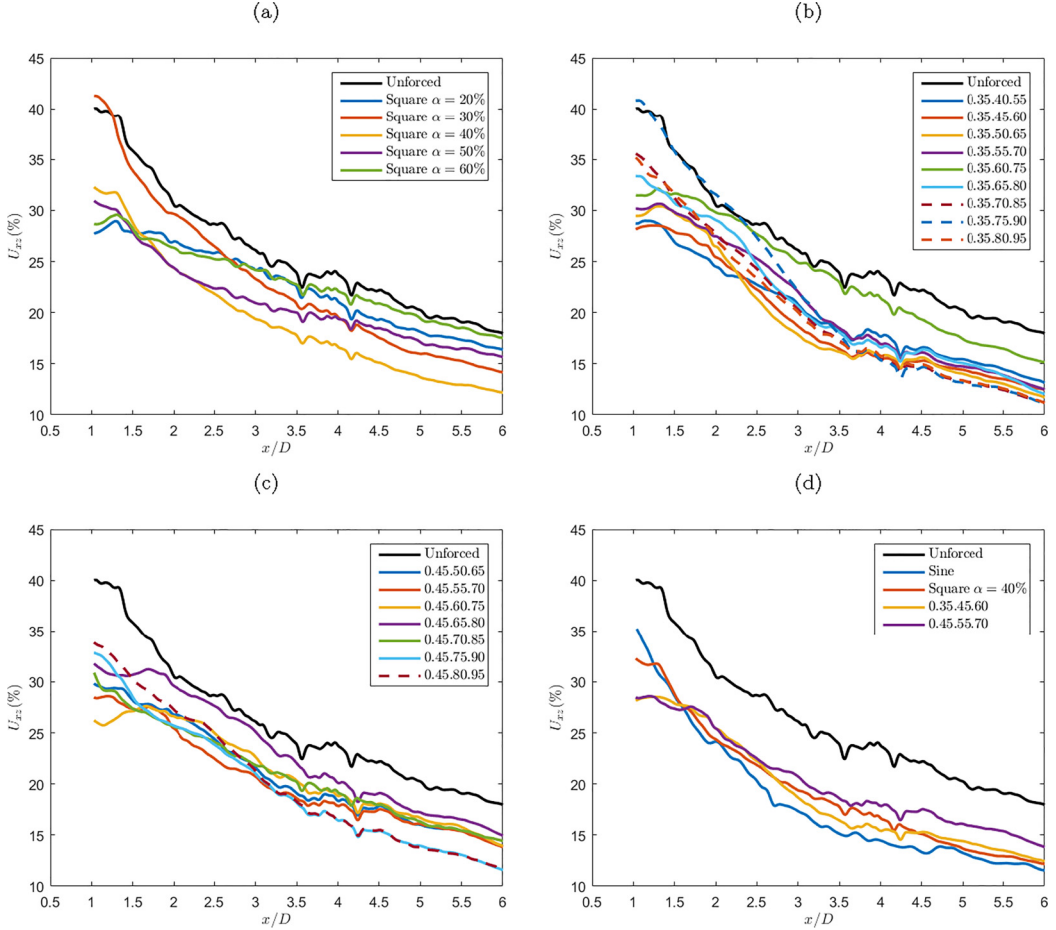
FIG. 16. Evolution of the centerplane unmixedness, U_{xz}, for a fixed excitation amplitude $u'_{j,\mathrm{rms}}/U_j = 0.50$ comparing: (a) $f_f = 110\,\mathrm{Hz}$ square waves with various duty cycles α, (b) double-pulse waveforms with the temporal pulse-widths fixed at $\tau_1/T = 0.35$ and $\tau_2/T = 0.15$, with variable temporal spacing between pulses, and (c) double-pulse waveforms with the temporal pulse-widths fixed at $\tau_1/T = 0.45$ and $\tau_2/T = 0.15$, with variable temporal spacing between pulses. Panel (d) summarizes differences in mixing for sinusoidal, square, and double-pulse excitation waveforms.

of $\tau_1/T = 0.45$, but still with $\tau_2/T = 0.15$, hence a longer "slow" pulse. For these excitation cases, there were similar observations to those in Fig. 16(b) in that a reduction in the temporal spacing between successive pulses created improved molecular mixing (e.g., cases 0.45.50.65 and 0.45.55.70).

Figure 16(d) provides comparisons of the mixing characteristics for the most effective temporal waveforms of all types (different double-pulse, square-wave, and sinusoidal waveforms) at the same forcing frequency. While all of the waveforms demonstrated remarkable improvement in the overall molecular mixing in the JICF as compared to an unforced flow, the sinusoidal waveform was the most effective at this applied forcing amplitude, which may be in part due to the propensity for the square and double pulse waveforms to generated a bifurcated flow, which in prior studies has been seen to be a less effective flowfield for mixing [37,39]. But the double-pulse excitation case with a relatively short temporal spacing, 0.35.45.60, provided similarly significant improvements in molecular mixing to those of sinusoidal excitation. The fact that the associated single-loop phase

portraits provided a characteristic signature that could be linked to these mixing improvements, in contrast to the multiple loop topologies associated with lesser mixing improvements could be of interest in further research exploration.

IV. DISCUSSION AND CONCLUSIONS

The present experimental study documented the effects of various axisymmetric excitation waveforms applied to a naturally absolutely unstable JICF at the momentum flux ratio $J = 6$. In this study, the response of the jet to excitation was documented in terms of the local and global evolution of the shear layer instabilities; the associated vorticity generation, evolution, and interactions in the jet nearfield; and overall jet structures, dynamical features, and associated molecular mixing. The study extended the parameter space explored in previous axisymetrically excited JICF studies, while taking advantage of diagnostics previously underutilized to present new perspectives on important known trends in the excitation waveforms.

Synchronization of the jet to applied excitation was explored for the AU jet with sinusoidal, square-wave, and double-pulse forcing waveforms, the latter of which involved slow and fast pulsations, enabling multiple vortical structures to be formed within a given forcing period and with the potential for strong and weak vortex interactions and collisions [39]. In the present study, both square and double-pulse square-wave excitation were created with differing numbers of underlying Fourier timescales, and for most cases with the full complement of Fourier modes (up to 15), it was easier to produce lock-in of the USL to excitation, especially as compared with sinusoidal excitation. In some of these cases there was over an 80% energy reduction in the required amplitude as compared with sine wave excitation. A related trend showed that a reduction in the number of Fourier terms used to create square and double-pulse waveforms increased the required excitation amplitude to achieve lock-in. Similarly, variation in the duty cycle of the applied square wave influenced the ability of the jet to synchronize with the forcing. These trends were the same as those found using an analogous Van der Pol oscillator model. In fact, the VdP oscillator model for square-wave excitation revealed that the proximity of the individual Fourier terms to the natural instability frequency, f_o, and their relative input strengths, controlled the synchronization of the jet far more than the coherence of the resulting square waveform.

The implications of synchronization characteristics of the transverse jet were explored further via optical diagnostics (simultaneous stereo PIV and acetone PLIF), with proper orthogonal decomposition (POD) modes extracted from centerplane velocity field measurements. Extensive comparisons among different excitation conditions were conducted; while the essential details are provided in this paper, many additional datasets are available in Harris [51]. In this paper, it was shown that sinusoidal forcing generated a slightly deeper penetrating jet as compared with double-pulse forcing, while double-pulse forcing generated a bifurcated jet structure. More importantly, at forcing amplitudes where both excitation waveforms were well past the state of LI, the sinusoidal forcing was represented by stronger and more coherent mode structures, while the double-pulse forcing produced a more complex and seemingly chaotic set of mode structures, owing to the induced nearfield vortex interactions and breakdown. Yet the degree of complexity in the double-pulse waveforms' POD mode shapes (and trajectories of their most energetic mode coefficients) was dependent on the temporal spacing between slow and fast pulses. Plots of the POD mode coefficients for the 3 most energetic modes produced fairly simple periodic (circular) shapes for sinusoidal excitation. In contrast, double-pulse forcing produced both single and multiple loop trajectories in their phase portraits, where the former were typically associated with relatively short temporal spacing between pulses and the latter were associated with longer spacing between slow and fast pulses. The distinctive character of the 3D phase portraits, involving the three most energetic POD modes, produced characteristic signatures associated with the various dynamical features of periodic vortical structures. Subsequent quantification of molecular mixing characteristics of the various excitation cases, via acetone PLIF, showed that the simpler phase portrait topologies, e.g., sinusoidal excitation and double-pulse square excitation with short temporal spacing between pulses [e.g., as

in Fig. 16(d)] tended to have improved molecular mixing as compared with other excitation cases, but all cases with excitation improved mixing over the unforced JICF case.

It is interesting that the mixing enhancement appeared to be related not just to the state of the resulting vortex rings (e.g., the degree of fill, as is typically the case for square-wave excitation [37]), but was also linked to the state of synchronization to the forcing and dynamical character of the most energetic modes, and related to the nearfield interactions of vortical structures. Remarkably, such correlations suggested that dynamical characteristics revealed through POD mode shapes and 3D coefficient plots could be used to develop characteristic signatures for transverse jet behavior that relate directly to their structure and scalar mixing characteristics. Such signatures could be especially beneficial in developing reduced-order models (ROMs) for the controlled jet in crossflow, an important component in the design of control algorithms in practical systems. Observations in the present study could indeed open the door to developing alternative ways by which to promote jet synchronization or more effectively generate nearfield vortex interactions, and these are the subject of ongoing explorations.

ACKNOWLEDGMENTS

[1] R. J. Margason, Fifty years of jet in cross flow research, in *Proceedings of the AGARD Symposium on Computational and Experimental Assessment of Jets in Crossflow* (AGARD, 1993), AGARD-CP-534.

[2] A. R. Karagozian, Transverse jets and their control, Prog. Energy Combust. Sci. **36**, 531 (2010).

[3] J. D. Holdeman, Mixing of multiple jets in a confined subsonic crossflow, Prog. Energy Combust. Sci. **19**, 31 (1993).

[4] S. V. Ekkad, S. Ou, and R. B. River, Effect of jet pulsation and duty cycle on film cooling from a single jet on a leading edge model, J. Turbomach. **128**, 564 (2006).

[5] P. J. Yagle, D. N. Miller, K. B. Ginn, and J. W. Hamstra, Demonstration of fluidic throat skewing for thrust vectoring in structurally fixed nozzles, ASME J. Eng. Gas Turb. Power **123**, 502 (2001).

[6] Y. Kamotani and I. Greber, Experiments on a turbulent jet in a cross flow, AIAA J. **10**, 1425 (1972).

[7] R. M. Kelso, T. T. Lim, and A. E. Perry, An experimental study of round jets in cross-flow, J. Fluid Mech. **306**, 111 (1996).

[8] A. R. Karagozian, The jet in crossflow, Phys. Fluids **26**, 101303 (2014).

[9] L. Cortelezzi and A. R. Karagozian, On the formation of the counter-rotating vortex pair in transverse jets, J. Fluid Mech. **446**, 347 (2001).

[10] K. Mahesh, The interaction of jets with crossflow, Annu. Rev. Fluid Mech. **45**, 379 (2013).

[11] E. Le Grives, Mixing process induced by the vorticity associated with the penetration of a jet into a cross flow, J. Eng. Power **100**, 465 (1978).

[12] J. E. Broadwell and R. E. Breidenthal, Structure and mixing of a transverse jet in incompressible flow, J. Fluid Mech. **148**, 405 (1984).

[13] L. Gevorkyan, T. Shoji, D. R. Getsinger, O. I. Smith, and A. R. Karagozian, Transverse jet mixing characteristics, J. Fluid Mech. **790**, 237 (2016).

[14] Z. M. Moussa, J. W. Trischka, and S. Eskinazi, The nearfield in the mixing of a round jet with a cross-stream, J. Fluid Mech. **80**, 49 (1977).

[15] Y. M. Marzouk and A. F. Ghoniem, Vorticity structure and evolution in a transverse jet, J. Fluid Mech. **575**, 267 (2007).

[16] T. F. Fric and A. Roshko, Vortical structure in the wake of a transverse jet, J. Fluid Mech. **279**, 1 (1994).

[17] S. Megerian, J. Davitian, L. de B. Alves, and A. R. Karagozian, Transverse-jet shear-layer instabilities. Part 1. Experimental studies, J. Fluid Mech. **593**, 93 (2007).

[18] J. Davitian, D. Getsinger, C. Hendrickson, and A. R. Karagozian, Transition to global instability in transverse-jet shear layers, J. Fluid Mech. **661**, 294 (2010).

[19] D. R. Getsinger, C. Hendrickson, and A. R. Karagozian, Shear layer instabilities in low-density transverse jets, Exp. Fluids **53**, 783 (2012).

[20] D. R. Getsinger, L. Gevorkyan, O. Smith, and A. R. Karagozian, Structural and stability characteristics of jets in crossflow, J. Fluid Mech. **760**, 342 (2014).

[21] T. Shoji, E. W. Harris, A. Besnard, S. G. Schein, and A. R. Karagozian, On the origins of transverse shear layer instability transition, J. Fluid Mech. **890**, A7 (2020).

[22] S. Bagheri, P. Schlatter, P. J. Schmid, and D. S. Henningson, Global stability of a jet in crossflow, J. Fluid Mech. **624**, 33 (2009).

[23] P. Schlatter, S. Bagheri, and D. S. Henningson, Self-sustained global oscillations in a jet in crossflow, Theor. Comput. Fluid Dyn. **25**, 129 (2011).

[24] P. S. Iyer and K. Mahesh, A numerical study of shear layer characteristics for low-speed transverse jets, J. Fluid Mech. **790**, 275 (2016).

[25] M. A. Regan and K. Mahesh, Global linear stability analysis of jets in cross-flow, J. Fluid Mech. **828**, 812 (2017).

[26] D. B. d. Souza, R. B. Freitas, and L. S. de B. Alves, Criterion for the linear convective to absolute instability transition of a jet in crossflow: The countercurrent viscous and round mixing layer analogy, Phys. Rev. Fluids **6**, L041901 (2021).

[27] P. Huerre and P. A. Monkewitz, Local and global instabilities in spatially developing flows, Annu. Rev. Fluid Mech. **22**, 473 (1990).

[28] L. Gevorkyan, T. Shoji, W. Y. Peng, and A. R. Karagozian, Influence of the velocity field on scalar transport in gaseous transverse jets, J. Fluid Mech. **834**, 173 (2018).

[29] M. A. Regan and K. Mahesh, Adjoint sensitivity and optimal perturbations of the low-speed jets in cross-flow, J. Fluid Mech. **877**, 330 (2019).

[30] E. W. Harris, A. Besnard, and A. R. Karagozian, Effect of tabs on transverse jet instabilities, structure, vorticity dynamics and mixing, J. Fluid Mech. **918**, A8 (2021).

[31] H. Johari, M. Pacheco-Tougas, and J. C. Hermanson, Penetration and mixing of fully modulated turbulent jets in crossflow, AIAA J. **37**, 842 (1999).

[32] R. T. M'Closkey, J. King, L. Cortelezzi, and A. R. Karagozian, The actively controlled jet in crossflow, J. Fluid Mech. **452**, 325 (2002).

[33] S. Shapiro, J. King, R. T. M'Closkey, and A. R. Karagozian, Optimization of controlled jets in crossflow, AIAA J. **44**, 1292 (2006).

[34] F. Muldoon and S. Acharya, Direct numerical simulation of pulsed jets in crossflow, Comput. Fluids **39**, 1745 (2010).

[35] R. Sau and K. Mahesh, Optimization of pulsed jets in crossflow, J. Fluid Mech. **653**, 365 (2010).

[36] J. Davitian, C. Hendrickson, D. Getsinger, R. T. M'Closkey, and A. R. Karagozian, Strategic control of transverse jet shear layer instabilities, AIAA J. **48**, 2145 (2010).

[37] T. Shoji, A. Besnard, E. W. Harris, R. T. M'Closkey, and A. R. Karagozian, Effects of axisymmetric square-wave excitation on transverse jet structure and mixing, AIAA J. **57**, 1862 (2019).

[38] T. Shoji, E. W. Harris, A. Besnard, and A. R. Karagozian, Effects of sinusoidal excitation on transverse jet dynamics, structure and mixing, AIAA J. **58**, 3889 (2020).

[39] E. W. Harris, T. Shoji, A. Besnard, S. G. Schein, R. T. M'Closkey, L. Cortelezzi, and A. R. Karagozian, Effects of controlled vortex generation and interactions in transverse jets, Phys. Rev. Fluids **7**, 013902 (2022).

[40] R. Sau and K. Mahesh, Dynamics and mixing of vortex rings in crossflow, J. Fluid Mech. **604**, 389 (2008).

[41] T. Shoji, E. W. Harris, A. Besnard, S. G. Schein, and A. R. Karagozian, Transverse jet lock-in and quasiperiodicity, Phys. Rev. Fuids **5**, 013901 (2020).

[42] L. K. B. Li and M. P. Juniper, Lock-in and quasiperiodicity in a forced hydrodynamically self-excited jet, J. Fluid Mech. **726**, 624 (2013).

[43] L. Gevorkyan, Structure and mixing characterization of variable density transverse jet flows, Ph.D. thesis, University of California, Los Angeles, 2015.

[44] T. Shoji, Mixing and structural characteristics of unforced and forced jets in crossflow, Ph.D. thesis, University of California, Los Angeles, 2017.

[45] H. Kantz and T. Schreiber, in *Nonlinear Time Series Analysis*, 2nd ed., edited by C. U. Press (Cambridge University Press, Cambridge, UK, 2003).

[46] F. Takens, Detecting strange attractors in turbulence, in *Dynamical Systems and Turbulence*, Lecture Notes in Mathematics, edited by D. Rand and L. S. Young (Springer, Berlin, Heidelberg, 1980), Vol. 898, pp. 366–381.

[47] Y. Guan, M. Murugesan, and L. K. B. Li, Strange nonchaotic and chaotic attractors in a self-excited thermoacoustic oscillator subjected to external periodic forcing, Chaos **28**, 093109 (2018).

[48] L. Cao, Practical method for determining the minimum embedding dimension of a scalar time series, Physica D **110**, 43 (1997).

[49] A. M. Fraser and H. L. Swinney, Independent coordinates for strange attractors from mutual information, Phys. Rev. A **33**, 1134 (1986).

[50] C. Hendrickson, Identification and control of the jet in crossflow, Ph.D. thesis, University of California, Los Angeles, 2012.

[51] E. W. Harris, Structure, mixing, and dynamics of controlled single and coaxial jets in crossflow, Ph.D. thesis, University of California, Los Angeles, 2020.

[52] A. Besnard, E. W. Harris, and A. R. Karagozian, Asymmetric forcing of convectively unstable transverse jets, Phys. Rev. Fluids **7**, 063902 (2022).

[53] P. V. Danckwerts, The definition and measurement of some characteristics of mixtures, Appl. sci. Res. **3**, 279 (1952).

[54] P. E. Dimotakis and P. L. Miller, Some consequences of the boundedness of scalar fluctuations, Phys. Fluids **2**, 1919 (1990).

[55] T. K. Caughey, Response of Van der Pol's oscillator to random excitation, J. Appl. Mech. **26**, 345 (1959).

[56] H. Simo and P. Woafo, Bifurcation structure of a Van der Pol oscillator subjected to nonsinusoidal periodic excitation, Int. J. Bifurcat. Chaos **22**, 1250003 (2012).

[57] L. Sirovich, Turbulence and the dynamics of coherent structures, Quart. Appl. Math. **45**, 561 (1987).

[58] K. E. Meyer, J. M. Pedersen, and O. Özcan, A turbulent jet in crossflow analysed with proper orthogonal decomposition, J. Fluid Mech. **583**, 199 (2007).